ChemistrySelect

Research Article
doi.org/10.1002/slct.202402762

Chemistry Europe
European Chemical Societies Publishing

www.chemistryselect.org

# Transition- and Lanthanide-Metal-Based Coordination Polymers Offer Efficient Methylene Blue Adsorption

Cresten Moodley,[a] Kaushik Mallick,[a] Alfred Muller,*[a] and D. Bradley G. Williams*[b]

This study presents a novel approach toward wastewater remediation via the synthesis of a series of coordination polymers that combine benzene-1,4-dicarboxylic acid, benzene-1,4-dihydroxamic acid, and 5-nitroisophthalic acid linkers with Cu, Cr, Ce, and La metal salts to target efficient methylene blue removal. Through a detailed characterization process using techniques like $^{1}$H NMR, PXRD, FTIR, TGA, SEM-EDX, ICP-OES, and BET, the structural and surface properties of these CPs were optimized for stability and enhanced adsorption performance. Notably, the CPs exhibited rapid MB adsorption within 10 min and followed pseudo-second-order kinetics, indicating a chemisorption-driven process. This work advances the field by demonstrating that increased pH significantly improves adsorption capacity and that the Sips model best describes the heterogeneous adsorptive behavior, highlighting a mixed Langmuir–Freundlich mechanism. Furthermore, stability and reusability studies revealed minimal metal leaching in the best-performing CPs, addressing critical environmental concerns around long-term CP use. This integrated approach not only fills vital knowledge gaps in CP-based dye adsorption kinetics but also underscores the potential of these materials as sustainable, scalable, and effective solutions for real-world water treatment applications.

## 1. Introduction

Global water resources face increasing threats from high demand across various domestic and industrial sectors, particularly leather, paper, and textile industries, which contribute significantly to water pollution through the discharge of dyes and other contaminants.[1] Untreated dye wastewater can undergo chemical and biological changes that reduce dissolved oxygen, harm aquatic ecosystems and present serious health risks to humans.[2] Effective dye removal from wastewater before discharge is therefore essential. This study will focus on the removal of methylene blue ($C_{16}H_{18}ClN_3S$), a heterocyclic thiazine dye that is widely used in textile, medicinal, and aquaculture industries (shown in Figure 1). Despite its long history of utility, methylene blue (MB) poses significant health and environmental risks. At elevated concentrations, MB can cause several harmful effects in humans, such as gastritis (nausea, vomiting, diarrhea) or more severe symptoms like dyspnea, tachycardia, cyanosis, or seizures. Furthermore, MB is non-biodegradable, which exacerbates its persistence in aquatic ecosystems, leading to long-term contamination of water bodies. These toxicological and environmental concerns have made the removal of MB from wastewater a critical priority, necessitating the development of effective remediation strategies, particularly in regions where MB is frequently used.[3–10]

Dye removal techniques typically fall into three categories: biological, chemical, or physical. Biological methods, though cost-effective and environmentally friendly, are limited by the metabolic capabilities of the microorganisms involved. Chemical methods, such as oxidative processes, are efficient but can produce secondary pollutants and often require expensive, specialized equipment. Physical methods, particularly adsorption, are widely preferred for their operational simplicity and limited chemical requirements, although the regeneration of adsorbents remains a challenge.[11]

Among physical adsorbents, activated carbon and zeolites are commonly used, yet each has limitations. Activated carbon offers high adsorption efficiency but requires energy-intensive regeneration, often through thermal or chemical treatments that increase costs and reduce sustainability over long-term use. Zeolites, while generally stable, have lower adsorption capacities for certain pollutants, such as anions or organics, and may encounter regeneration issues based on the type of adsorbate and environmental conditions.[12–17] Coordination polymers (CPs), constructed from metal ions and organic linkers, present a promising alternative due to their high porosity, large surface areas, and versatility for post-synthetic modifications that enhance adsorption performance and stability.[18–20] CPs offer selective adsorption properties and recyclability, making them promising candidates for dye removal applications.

However, CP stability in aqueous environments remains a challenge, as metal-linker bond hydrolysis can compromise

[a] C. Moodley, K. Mallick, A. Muller
University of Johannesburg, Department of Chemical Sciences, Auckland Park, P.O. Box 524, Johannesburg, South Africa
E-mail: mullera@uj.ac.za

[b] D. B. G. Williams
University of Wollongong, School of Chemistry and Molecular Bioscience, Wollongong, New South Wales 2522, Australia
E-mail: bradleywi@uow.edu.au

Supporting information for this article is available on the WWW under https://doi.org/10.1002/slct.202402762

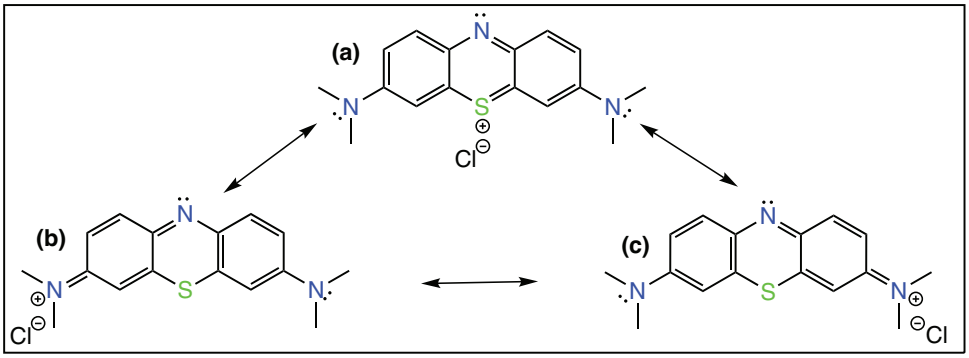


**Figure 1.** Resonance structures of cationic methylene blue (MB) with chloride counterion.

structural integrity, especially under harsh conditions.[21] This hydrolysis often leads to metal leaching, raising particular concerns with lanthanides. Though lanthanides are generally considered less toxic than heavy metals, ecotoxicological data are limited, with most research focusing on cerium and lanthanum. Interestingly, lanthanides at low concentrations can stimulate growth in certain microalgae by potentially replacing essential metals in physiological roles, such as alleviating $Ca^{2+}$ deficiency. However, their effect is highly dependent on the organism's physiological state. The same lanthanide concentration may act as a growth stimulant or, under certain stress conditions, become toxic and inhibit growth, which raises interest about the broader environmental safety of lanthanides at low concentrations. Furthermore, lanthanides are known to accumulate in sediments, posing potential risks to sediment-dwelling and sediment-ingesting species. Notable bioaccumulation in some aquatic plants further emphasizes the need for detailed research on lanthanide behavior and impacts across food chain levels to accurately assess their environmental impact.[22,23]

In addition to stability, the economic viability of CP adsorbents for large-scale applications remains challenging due to high synthesis costs, preparation complexity, and limitations in producing handleable, industrially suitable forms. Currently, CPs are synthesized primarily as powders in small, gram-scale quantities, which are expensive and difficult to deploy outside of laboratory settings.[24,25] Successful deployment requires not only scalable, cost-effective synthetic methods but also eco-friendly approaches that take environmental impact, component availability, and toxicity into account. Even with high retail prices, the potential of CPs to outperform commercially available adsorbents in terms of selectivity, capacity, and durability could drive market demand, incentivizing further research and investment in this field. Optimizing synthesis routes to control morphology and particle size to ensure batch reproducibility is crucial for cost reduction. Currently, batch synthesis is the most viable industrial production method, but advancements in continuous synthesis methods could further improve scalability. Ensuring sustainable industrial use of CPs will require strong collaboration between academia and industry to bring CP-based technologies to market effectively.[26,27]

Transition-metal-based CPs, such as MIL-101 (Cr), UiO-66 (Zr), and MOF-235 (Fe), have been effectively utilized to remove MB from wastewater due to their high surface areas and stability.[28–30] Cost-effective linkers like benzene-1,4-dicarboxylic acid (BDC) support the formation of stable porous frameworks, and modifications such as converting BDC to benzene-1,4-dihydroxamic acid (BHA) can enhance stability and adsorption efficiency. Additionally, incorporating electron-withdrawing groups like the nitro group (—$NO_2$) in linkers such as 5-nitroisophthalic acid (5NIP) may boost CP performance in harsher environments.[31–33] Studies on BHA- and 5NIP-based CPs have primarily focused on mixed linker systems used for photocatalytic dye degradation or as collectors in mineral processing applications.[34–37]

To tackle these challenges, the present study focuses on preparing mono-linker-based CPs using BDC, BHA, and 5NIP linkers combined with lanthanum (La), cerium (Ce), copper (Cu), and chromium (Cr) metal ions, resulting in twelve CP variants specifically designed for effective MB adsorption. The CPs produced here not only facilitate the removal of MB from wastewater but also allow for the potential recycling of the adsorbed dye. Such capture-recover methods underscore the advantages of adsorption over photodegradation, the latter of which could possibly generate unintended secondary pollutants. La and Ce were selected for their high coordination numbers and stability, while Cu and Cr were chosen for their favorable chemical properties and cost-effectiveness.[38–45] By integrating these specific metals with functionalized linkers, we aim to develop CPs that exhibit enhanced stability, high adsorption capacity, and minimal metal leaching to advance sustainable wastewater treatment technologies.

## 2. Results and Discussion

### 2.1. Synthesis of Coordination Polymers

The solvothermal synthesis of the CPs involved the independent dissolution of the metal nitrate hydrate salts and the linkers (shown in Figure 2) in DMF and mixing thereof in a PTFE-lined stainless-steel vessel. The contents of the vessels were stirred using a magnetic follower, and once homogeneous, the vessel was sealed tightly. It was heated using a silicone oil bath according to a programmed heating cycle without stirring, from room temperature to 120 °C, at a ramp rate of 5 °C/min. The vessel was

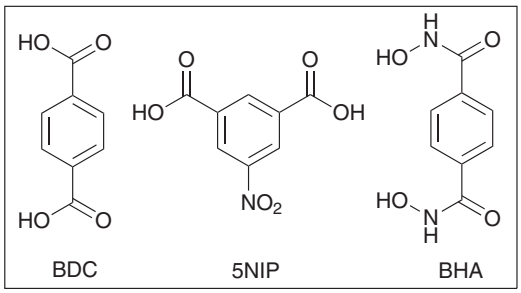


**Figure 2.** Structures of BDC, 5NIP, and BHA used as CP organic linkers in this study.

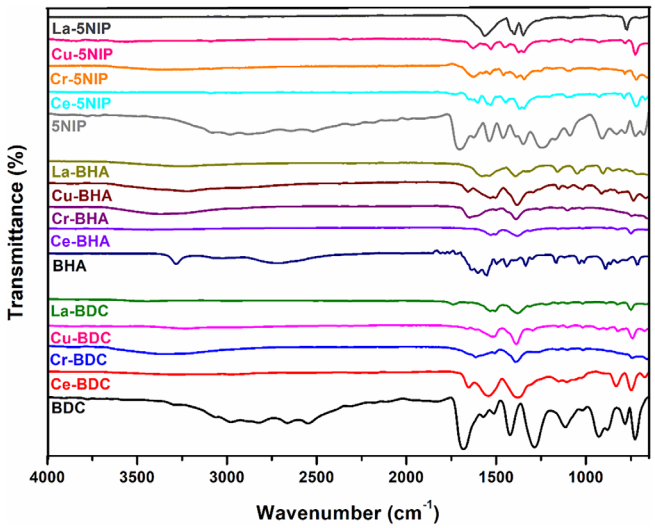


**Figure 3.** Stacked FTIR spectra of the BDC, BHA, and 5NIP linkers with their corresponding CPs.

maintained at this temperature for 72 h and then cooled to room temperature at a rate of 5 °C/min. The solid material formed inside the vessel was filtered through a Buchner funnel, washed with DMF to remove unreacted starting material, and then sequentially washed with distilled $H_2O$ and MeOH to remove the DMF. The filtered material was dried under high vacuum ($2 \times 10^{-3}$ mbar at 100 °C for 12 h) prior to characterization.

## 2.2. Characterization of the Coordination Polymers

### *2.2.1. Infrared Spectroscopy*

The FTIR spectra of the CPs of BDC, BHA, and 5NIP (shown in Figure 3) were used to assess the characteristic functional group stretching frequencies. The wavenumber separation ($\Delta\upsilon$) between the asymmetric ($\upsilon_{asym}$ ($cm^{-1}$), asymmetric $COO^-$ stretching frequency) and symmetric ($\upsilon_{sym}$ ($cm^{-1}$), symmetric $COO^-$ stretching frequency) vibrations of the deprotonated carboxylic ($COO^-$) moieties found in BDC and 5NIP linkers was calculated using Equation (1) (summarized in Table 1). The simple yet powerful $\Delta\upsilon$ approach permits the identification of the carboxylate-metal coordination type.[46–48] In particular, $\Delta\upsilon < 110$ $cm^{-1}$ implies a chelating mode of binding, $> 140$ $cm^{-1}$ is indicative of a bridging bidentate mode of binding, and $> 200$ $cm^{-1}$ denotes a monodentate binding mode.

$$\Delta\upsilon = \upsilon_{asym}\left(COO^-\right) - \upsilon_{sym}\left(COO^-\right) \quad (1)$$

The FTIR spectra of the BDC-CPs and 5-NIP CPs displayed broad, low-intensity bands at 2800–3600 and 2357–3313 $cm^{-1}$ assigned to O—H stretching frequencies of coordinated $H_2O$ in the system, consistent with results obtained during thermogravimetric analysis (see below). Furthermore, the CPs derived from BDC and 5NIP were devoid of the CO—H stretch at 1286 and 1242 $cm^{-1}$, respectively, which indicated coordination via deprotonation of both carboxylic OH groups present in the free linkers.[49–51] The BDC-CPs and 5NIP-CPs displayed shifted carbonyl double bond C=O stretching frequencies at 1691 and 1687 $cm^{-1}$, respectively, with corresponding appearances of C—O asymmetric and symmetric stretches.[52–53] The FTIR spectra of the BHA-CPs displayed a decrease in the intensity of the C=O band and the strong NH and O—H stretching vibrations occurring at 1601, 3285, and 2900–2400 $cm^{-1}$ in the free BHA linker, indicating metal coordination via these moieties.[54] The FTIR spectra were devoid of bands associated with DMF, indicating complete removal thereof during the purification of the CPs.

### *2.2.2. ICP-OES Analysis*

ICP-OES analysis was conducted on the synthesized CPs to determine both the metal content (wt%) and the metal-to-linker (M/L) ratio (summarized in Table 2). For the lanthanide-based CPs, a 1:1.5 metal-linker ratio was observed, whereas a 1:1 ratio was noted for the transition metal-based CPs. Consistent with expectations, the metal content by weight decreased with the use of higher molecular weight ($M_W$) linkers, likely because larger linkers occupy more space in the CP framework and reduce the number of metal ions that could be incorporated per unit mass of the CP. In wastewater treatment, a higher metal content in CPs often increases active site availability, which enhances dye adsorption interactions, improving the efficiency of the removal of the dye. Therefore, careful linker selection is essential for balancing structural stability with metal loading to create effective adsorbents for dye-laden wastewater.[55,56]

### *2.2.3. Thermal Analysis*

Thermogravimetric analysis (TGA) was used to assess the thermal stability of the respective CPs. The thermograms of the three linker systems (BDC, BHA, and 5NIP) revealed rapid decomposition beyond ca. 200 °C. Both BDC and 5NIP underwent complete decomposition around 350 °C, while BHA displayed greater thermal stability, decomposing fully at around 550 °C. The thermograms for the CPs were compared with their corresponding linkers (shown in Figure S1) and displayed initial weight losses up to 150 °C attributed to the loss of water molecules. The decomposition of the CPs occurred more gradually, indicating that the M-L coordination provided enhanced thermal stability. The decomposition profiles of the CPs typically fol-

**Table 1.** Summary of $COO^-$ symmetric and asymmetric stretches, $\Delta\upsilon$, and associated coordination modes observed for the BDC- and 5NIP-CPs.

| CP | C═O ($cm^{-1}$) | C—OH ($cm^{-1}$) | $COO^-_{asym}$ ($cm^{-1}$) | $COO^-_{sym}$ ($cm^{-1}$) | $\Delta\upsilon$ ($cm^{-1}$) | Carboxylate-Metal Coordination Type |
|---|---|---|---|---|---|---|
| BDC | 1684 | 1286 | – | – | – | – |
| Ce-BDC | – | – | 1660 | 1373 | 287 | Monodentate |
| Cr-BDC | – | – | 1565 | 1379 | 186 | Bridging-bidentate |
| Cu-BDC | – | – | 1581 | 1392 | 189 | Bridging-bidentate |
| La-BDC | – | – | 1581 | 1379 | 202 | Monodentate |
| 5NIP | 1702 | 1461 | – | – | – | – |
| Ce-5NIP | – | – | 1521 | 1420 | 101 | Chelating |
| Cr-5NIP | – | – | 1530 | 1420 | 110 | Chelating |
| Cu-5NIP | – | – | 1521 | 1420 | 101 | Chelating |
| La-5NIP | – | – | 1560 | 1398 | 162 | Bridging-bidentate |

**Table 2.** Metal-to-linker (mol/mol) ratio based on ICP-OES data.

| L | Ce/L | Ce (wt%) | Cr/L | Cr (wt%) | Cu/L | Cu (wt%) | La/L | La (wt%) |
|---|---|---|---|---|---|---|---|---|
| BDC | 1:1.5 | 56 | 1:1 | 32 | 1:1 | 35 | 1:1.5 | 56 |
| BHA | 1:1.5 | 48 | 1:1 | 29 | 1:1 | 30 | 1:1.5 | 48 |
| 5NIP | 1:1.5 | 47 | 1:1 | 26 | 1:1 | 27 | 1:1.5 | 45 |

**Table 3.** Structural calculations from the thermograms for the solvent-free BDC-, BHA-, and 5NIP- CPs.

| CP | Residue (%) | Metal Oxide ($M_W$) | Linker (%) | Linker ($M_W$) | M/L |
|---|---|---|---|---|---|
| Ce-BDC | 33 | **$CeO_2$ (172.12)** | 49 | 166.13 | 1:1.5 |
| Ce-BHA | 32 | | 55 | 196.16 | 1:1.5 |
| Ce-5NIP | 30 | | 54 | 211.13 | 1:1.5 |
| Cr-BDC | 26 | **$Cr_2O_3$ (151.99)** | 59 | 166.13 | 1:1 |
| Cr-BHA | 22 | | 60 | 196.16 | 1:1 |
| Cr-5NIP | 20 | | 58 | 211.13 | 1:1 |
| Cu-BDC | 14 | **$Cu_2O$ (143.09)** | 33 | 166.13 | 1:1 |
| Cu-BHA | 23 | | 64 | 196.16 | 1:1 |
| Cu-5NIP | 27 | | 80 | 211.13 | 1:1 |
| La-BDC | 38 | **$La_2O_3$ (325.81)** | 58 | 166.13 | 1:1.5 |
| La-BHA | 30 | | 55 | 196.16 | 1:1.5 |
| La-5NIP | 30 | | 58 | 211.13 | 1:1.5 |

lowed a slower, multi-step process likely involving organic linker degradation.

Metals typically do not volatilize under TGA conditions. Accordingly, the residual mass observed at the end of the TGA analysis usually can be reliably attributed to metal oxides.[57–61] The amount of residual metal oxides following CP degradation in the TGA instrument was used to calculate the metal to linker (M/L) ratio of the CPs (summarized in Table 3) and corresponded to the M/L ratios determined by ICP-OES.[62]

### 2.2.4. SEM-EDX Analysis

Scanning electron microscopy (SEM) is a non-destructive and efficient technique for analyzing properties such as crystal size, morphology, and elemental composition. SEM provides 2D surface images and may not accurately represent true 3D crystal sizes, which can be influenced by agglomeration, surface roughness, or porosity, and which vary based on material properties, surface energy, and synthetic conditions that affect grain size, growth, densification, and overall shape.[63–65]

Energy dispersive X-ray (EDX) spectroscopy is used in conjunction with SEM to determine the elemental composition by capturing X-rays generated when the electron beam strikes the sample. Although this method can indicate elemental distribution and purity, elemental composition should be confirmed with techniques like ICP-OES.[66,67]

In this study, CP samples were spin-coated with graphite to reduce image distortions during SEM imaging, and the resulting SEM images were analyzed to evaluate the morphology and dimensions of individual CP particles (summarized in Tables S2 and S3), while EDX was employed to ascertain the metallic composition (shown in Figures S2–S13). The CPs predominantly exhibited plate-like structures, indicative of 2D anisotropic growth. In contrast, Cr-BDC and Cu-BDC displayed needle-like morphologies, signifying 1D growth, whereas La-BDC showed spherical shapes characteristic of isotropic growth. These morphological differences provide insights into bonding characteristics, that is, strong in-plane bonding in plate-like structures, strong elongation bonding in needle-like forms, and uniform bonding in spherical shapes.[68–72] Aggregative behavior was noted for Ce-BDC, Cr-BDC, Cr-5NIP, and Cu-5NIP, appearing as cohesive entities made up of multiple indistinct particles. The remaining CPs exhibited agglomerative behavior, characterized by loosely interconnected clusters. Particle dimensions generally ranged from 1 to 2 µm, although accurate measurements for the Cr-, Cu-, and La-5NIP CPs were hindered by their sheet morphology. EDX analysis confirmed the presence of anticipated metals in the CPs and validated the absence of contaminants, ensuring the accuracy of metal content quantification via ICP-OES (see Section 2.2.2).[73,74]

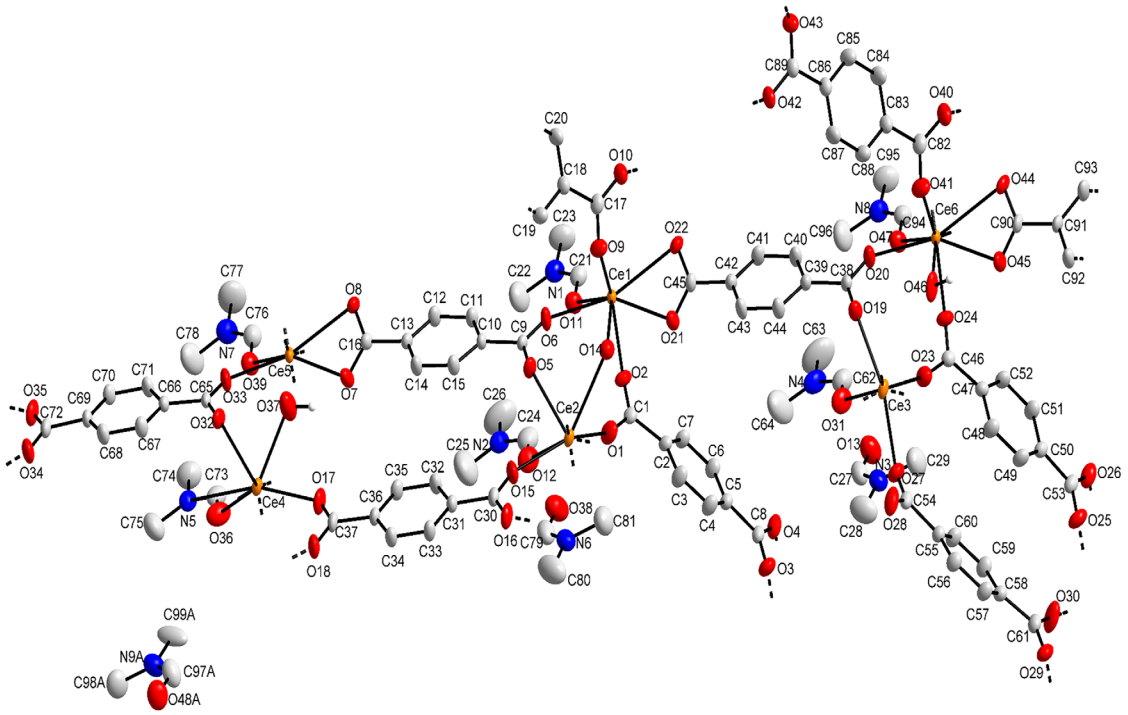


**Figure 4.** A view of the molecular structure with atom labelling of Ce-BDC in the asymmetric unit. The displacement ellipsoids are drawn at the 50% probability level with symmetry-generated atoms indicated by dotted bonds. Disorder on hydrogen atoms and DMF was omitted for clarity.

### *2.2.5. Single Crystal X-Ray Diffraction*

Colorless Ce-BDC crystals suitable for single-crystal X-ray diffraction (SC-XRD) crystallography were obtained directly from the solvothermal synthesis and were similar to the Ce-BDC crystals reported by the slow diffusion method.[75] In brief, the Ce-BDC crystallized in a triclinic space group $P_{\bar{1}}$ with an asymmetric unit comprised of six Ce (III) ions bound to a total of nine deprotonated BDC linkers having the molecular formula $[Ce_6(BDC)_9(DMF)_6(H_2O)_3{\cdot}3DMF]_n$ (shown in Figure 4).

The deprotonated BDC linkers coordinated to the Ce (III) ions in one of two coordination modes within the same system. In the first coordination mode, there are four bridging BDC linkers and one chelating BDC linker, while in the second mode, there are six bridging BDC linkers to balance the charge on each Ce (III) ion. As the Ce-BDC crystals were obtained before the washing and vacuuming step, the coordination spheres are completed by the presence of a single DMF ligand (shown in Figure 4). Furthermore, the asymmetric unit is comprised of three water molecules, whereby one was $\mu_2$-bridged ($Ce_1$—$O_{14}$—$Ce_2$) and the remaining two were directly coordinated ($Ce_4$—$O_{37}$ and $Ce_6$—$O_{46}$) to a Ce center. Both the coordinated/bridged $H_2O$ and coordinated DMF did not contribute toward the overall charge of the Ce (III) ion (summarized in Table S4a). It should be noted that the washing and vacuum steps previously discussed (see above) were shown to completely remove the DMF from the solids. In the present instance, the procedure does not include those steps, and the DMF and $H_2O$ were retained as ligands. The asymmetric unit contained six crystallographically distinct Ce (III) centers (shown in Figure 5), exhibiting two coordination types. $Ce_1$ and $Ce_6$ were eight-coordinate, bonded to eight oxygen atoms from one chelating carboxylate group, four bridging carboxylate groups, one terminal DMF molecule, and one water molecule. Similarly, $Ce_2$ and $Ce_4$ were also eight-coordinate, but with eight oxygen atoms from six bridging carboxylate groups, one terminal DMF molecule, and one water molecule. Although both $Ce_3$ and $Ce_5$ are seven-coordinate, $Ce_3$ is connected to seven oxygen atoms from six bridging carboxylate groups and one terminal DMF molecule, whereas $Ce_5$ is connected to seven oxygen atoms coming from one chelating carboxylate group, four bridging carboxylate groups, and one terminal DMF molecule.

### *2.2.6. Powder X-Ray Diffraction*

Powder X-ray diffraction (PXRD) was employed to assess the crystallinity, phase purity, and structural integrity of the synthesized CPs (shown in Figure 6 and summarized in Table 4). The experimental PXRD patterns of the washed CPs (see Section 2.1) were compared with those of their synthesis precursors (nodes and linkers) and simulated spectra derived from available single-crystal data in the CSD, providing insights into each CP's stability and phase composition. To confirm the reliability of the comparative PXRD approach, experimental spectra of the crystalline linkers BDC and 5NIP were first compared with their simulated spectra (shown in Figure S14), showing strong alignment and supporting the method's accuracy. Although no crystal data were available for BHA in the CSD, its experimental PXRD spectrum was still useful for evaluating its corresponding CPs. In some cases, multiple CSD datasets were available for selected CPs, and the simulated spectra dataset with the closest alignment to the experimental diffractogram was chosen for

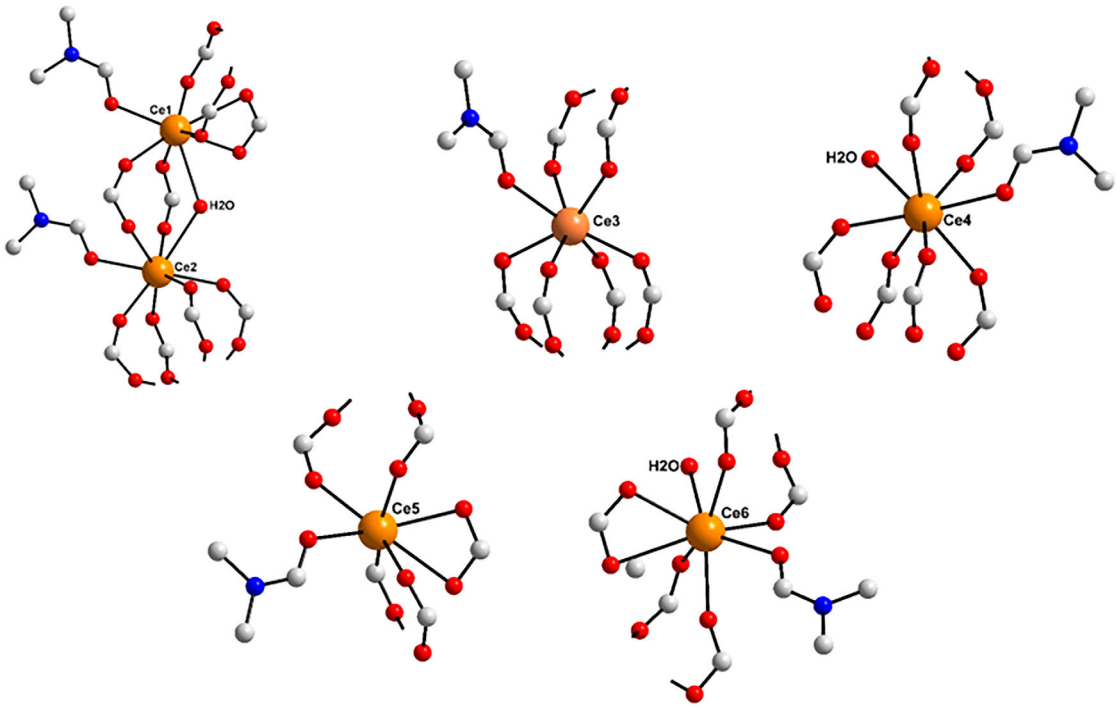


**Figure 5.** Coordination spheres of $Ce_1$–$Ce_6$ as observed in the asymmetric unit of Ce-BDC.

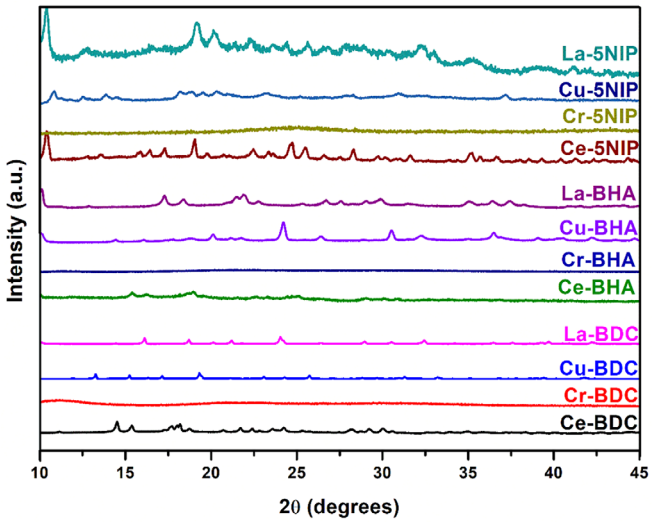


**Figure 6.** Stacked PXRD diffractograms of the washed BDC-, BHA-, and 5NIP-CPs.

analysis. Simulated PXRD patterns were generated for Ce-BDC, Ce-BHA, Cr-BDC, Cu-BDC, Cu-5NIP, La-BDC, and La-5NIP CPs. Due to the isostructural nature of Ce-5NIP and La-5NIP, the simulated La-5NIP spectrum was used to identify characteristic $2\theta$ peaks for the experimental Ce-5NIP CP. For most CPs, the experimental spectra showed a close match to $2\theta$ diffraction peaks in the simulated patterns, which supported the phase purity and structural integrity of the microcrystalline materials. Minor discrepancies observed in $2\theta$ peaks for some microcrystalline CPs may be due to factors like internal stresses, twin boundaries, stacking faults, chemical heterogeneities, or slight structural defects. Ce-BHA, however, was an exception with its experimental PXRD spectrum deviating from the simulated one despite certain matching peaks, suggesting possible variations in structural parameters or packing arrangements. The Cr-based CPs exhibited an amorphous nature, likely due to synthesis conditions such as temperature, pH, reaction time, or steric constraints that may have restricted crystallite formation.[54,76–86] The M/L ratios of CPs that aligned well between experimental and simulated PXRD patterns were consistent with the stoichiometries obtained via ICP-OES analysis (Section 2.2.2), further supporting the structural integrity of these CPs. However, the M/L ratio of Ce-BHA deviated from expected values, highlighting that even for CPs composed of identical metal and linker components, differences in stoichiometry can significantly impact structural phases, unit cell parameters, and framework topology.[87]

### 2.2.7. Gas Sorption

***BET experimental:*** The $N_2$ adsorption isotherms of the CPs were evaluated to identify isotherm types, surface area, and pore size distribution (summarized in Table S6). Cu-5NIP, Cu-BHA, and La-5NIP displayed type II isotherms, indicative of multilayer adsorption, and broad pore distribution, with BET surface areas of La-5NIP (79.9 $m^2\ g^{-1}$) > Cu-BHA (64.3 $m^2\ g^{-1}$) > Cu-5NIP (36.9 $m^2\ g^{-1}$) and pore diameters of Cu-5NIP (18 nm) > Cu-BHA (12 nm) > La-5NIP (6 nm). Higher surface areas are typically correlated with enhanced adsorption capacity for gases and dyes.[88–90] The remaining CPs exhibited type III isotherms, signifying weaker adsorbate–adsorbent interactions and multilayer formation. BET constant ($C$) values for type II CPs suggested moderate interactions ($50 \leq C < 500$), whereas type III CPs

**Table 4.** Summary of 2$\theta$ (°) peaks in experimental and simulated diffractograms of microcrystalline CPs.

| CP | Experimental CP versus (simulated CP*) 2$\theta$ Peaks |
|---|---|
| Ce-BDC | 11.2 (11.3); 15.4 (15.5); 17.6 (17.7); 18.0 (18.0); 21.7 (21.7); 22.4 (22.4); 22.8 (22.8); 23.5 (23.5); 28.1 (28.1); 28.7 (28.7); 29.2 (29.2); 30.0 (29.9); 30.6 (30.7); 34.9 (35.0); 37.2 (37.2); 38.4 (38.4) |
| Ce-BHA | 15.2 (15.3); 19.6 (19.6); 22.4 (22.5); 23.4 (23.5); 24.5 (24.5); 31.0 (30.9) |
| Ce-5NIP | 10.3 (10.3); 12.8 (12.8); 19.1 (19.1); 20.1 (20.0); 21.4 (21.4); 22.3 (22.4); 23.6 (23.6); 24.5 (24.5); 25.4 (25.6); 32.1 (32.0); 32.9 (33.0); 35.3 (35.3); 43.3 (43.4) |
| Cr-BDC<br>Cr-BHA<br>Cr-5NIP | Amorphous |
| Cu-BDC | 12.0 (12.0); 17.1 (17.1); 20.4 (20.5); 21.1 (21.1); 29.3 (29.3); 30.4 (30.4); 31.0 (31.0); 31.3 (31.3); 34.3 (34.3); 35.0 (35.0); 36.8 (36.8); 37.8 (37.8); 41.6 (41.7) |
| Cu-BHA | 15.9; 17.7; 18.8; 24.2; 26.4; 30.4; 32.3; 36.4; 39.1; 40.5; 42.3 |
| Cu-5NIP | 11.7 (11.7); 18.5 (18.5); 19.6 (19.6); 23.3 (23.3); 25.3 (25.3); 26.6 (26.6); 28.1 (28.1); 31.0 (31.0); 32.6 (32.6) |
| La-BDC | 16.2 (16.2); 18.7 (18.8); 20.1 (20.1); 21.1 (21.1); 25.5 (25.5); 25.8 (25.8); 26.3 (26.4); 29.0 (29.0); 30.6 (30.6); 32.4 (32.4); 34.2 (34.2); 37.7 (37.8); 39.8 (39.8); 42.2 (42.2) |
| La-BHA | 17.3; 18.4; 21.6; 22.8; 25.3; 29.9; 31.1; 36.4; 37.4 |
| La-5NIP | 12.9 (12.9); 15.1 (15.1); 20.1 (20.0); 26.3 (26.2); 27.4 (27.5); 29.6 (29.5); 31.2 (31.2); 32.8 (32.8); 33.4 (33.3); 33.5 (33.6); 35.3 (35.3); 37.1 (37.1); 39.8 (39.9) |

**Table 5.** Aromatic proton shifts of BDC, BHA, 5NIP, and their respective CPs using $CD_3COOD$ in DMSO-$d_6$.

| CP | BDC (ppm) | BHA (ppm) | 5NIP (ppm) |
|---|---|---|---|
| Ce | 8.10 ($H_a$, s, 4H) | 7.85 ($H_a$, s, 4H) | 8.87 ($H_b$, s, 1H), 8.82 ($H_a$, s, 2H) |
| Cr | 7.96 ($H_a$, s, 4H) | Paramagnetic | Paramagnetic |
| Cu | 7.97 ($H_a$, s, 4H) | 7.85 ($H_a$, s, 4H) | 8.63 ($H_b$, s, 1H), 8.62 ($H_a$, s, 2H) |
| La | 7.80 ($H_a$, s, 4H) | 7.86 ($H_a$, s, 4H) | 8.73 ($H_a$, s, 2H), 8.71 ($H_b$, s, 1H) |
| Linker | 8.01 ($H_a$, d, 4H) | 7.90 ($H_a$, s, 4H) | 8.74 ($H_a$, s, 2H), 8.68 ($H_b$, s, 1H) |

indicated weaker interactions ($1 \leq C < 50$). Interestingly, La-BHA ($C = 52$) and Cu-BDC ($C = 134$) showed type III isotherms despite $C$ values associated with type II behavior, possibly due to heterogeneity or edge effects. $N_2$ desorption isotherms further classified CPs into type III (Cr-BDC), IV (Ce-BDC, Cu-BDC, La-BDC, Ce-5NIP, Cr-5NIP, Cu-5NIP, La-5NIP, Ce-BHA, Cu-BHA, La-BHA), and V (Cr-BHA) behaviors. The type IV/V isotherms exhibited $H_3$ hysteresis loops, characteristic of materials with non-rigid, groove-shaped mesoporous (2–50 nm) to macroporous (>50 nm) structures.[91–92]

***BJH theory:*** BJH theory was applied to analyze the pore characteristics of BDC-, BHA-, and 5NIP-CPs (summarized in Table S7) using isotherm data within a pore width range of 17–3000 Å. Consistent surface area, pore volume, and pore diameter from both adsorption and desorption isotherms indicated surface uniformity in Cr-BDC, Cr-BHA, Cr-5NIP, and La-BHA enhancing the reliability of pore size distribution data and allowing accurate characterization.[93–95] In contrast, minor deviations between adsorption and desorption isotherms were observed for La-BDC, Ce-BDC, Cu-BDC, Ce-5NIP, Cu-5NIP, La-5NIP, and Cu-BHA, possibly attributed to differences in pore structure, limited adsorbate accessibility, or non-uniform pore size distribution suggestive of surface heterogeneity. The average pore diameter across the CPs ranged from 6 to 38 nm, consistent with mesoporous materials, in agreement with BET analysis.[96,97]

**t-*Plot experimental:*** The characteristics of the *t*-plot curves, micropore volumes, and external surface areas for the CPs were analyzed (shown in Figures S30–S41 and summarized in Table S8). At low relative pressures, the CPs did not exhibit micropore filling, as evidenced by the absence of distinct linear regions in their *t*-plots. Instead, the observed straight-line curves with positive gradients indicated that the amount of adsorbed gas increased proportionally with statistical thickness, characteristic of multilayer adsorption on a relatively uniform mesoporous surface with consistent adsorption energy, where each additional layer of gas molecules is adsorbed with similar energy.[98] Notably, the *t*-plot curve for La-5NIP displayed a straight line with a positive gradient that tapered into a gentler slope at higher statistical thickness, suggestive of rapid micropore filling initially (steep gradient reflecting significant microporosity and high adsorption potential) which transitioned into multilayer adsorption in larger pores (gentle gradient reflecting mesoporosity with lower adsorption potential and capillary condensation).[99,100] Although the La-5NIP curve did not completely flatten, the decreasing gradient at higher statistical thickness indicated pore filling saturation due to limited pore volume. The micropore volumes calculated were negative, suggestive of limited microporosity reinforcing the mesoporous nature of the CPs.[101] The external surface areas of the CPs were determined using the H–J model from the slope of the linear regions in the *t*-plots (where slope $\propto$ external surface area) and showed good agreement with the BET surface area values (Table S9).[102] However, the *t*-plot-derived external surface areas were consistently higher than the BET reported values, possibly due to nitrogen compressibility within micropores, where the *t*-plot model tends to underestimate micropore volume while overestimating external surface area.[103]

### 2.2.8. Digestive $^1$H NMR Spectroscopy

$^1$H NMR was performed on the CPs under digestive conditions using $CD_3COOD$ in DMSO-$d_6$ (shown in Figures S43–S55). The aromatic proton signals (summarized in Table 5) observed under these conditions are consistent with the parent ligands, indicating that the integrity of the linkers is preserved in the solvothermal synthesis method. The absence of residual DMF peaks supports the complete removal thereof during CPs purification, agreeing with FTIR analysis.

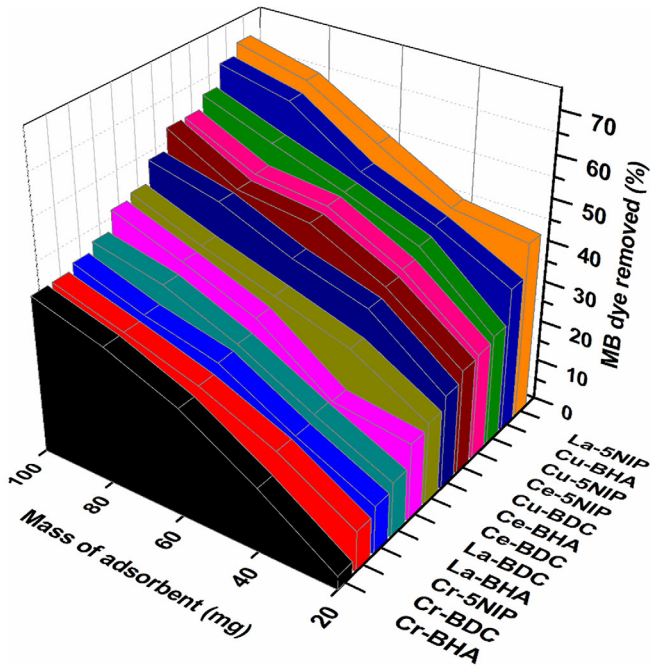


**Figure 7.** The effect of adsorbent loading on MB dye adsorption (pH 6.8, concentration 30 mg $L^{-1}$, time 60 min, CP loading 20–100 mg, 298 K).

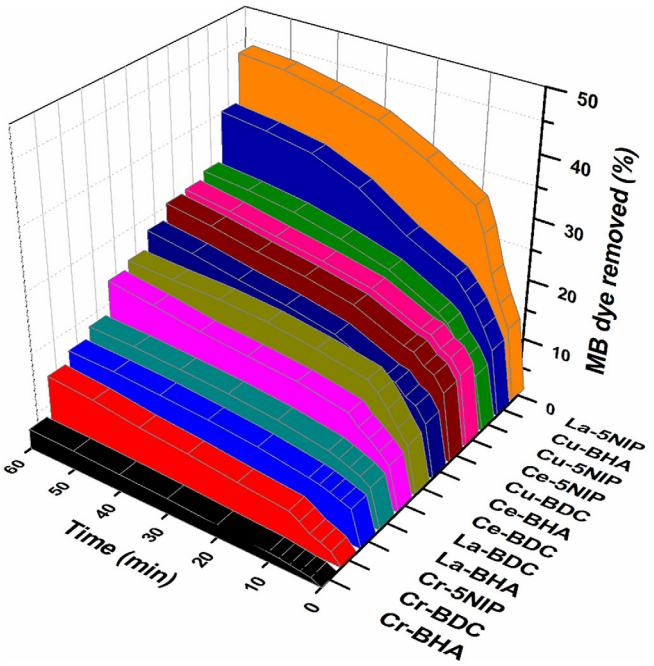


**Figure 8.** The effect of contact time for the adsorption of MB onto the respective CPs (pH 6.8, MB concentration of 30 mg $L^{-1}$, time 60 min, CP loading of 20 mg, 298 K).

## 2.3. Methylene Blue (MB) Adsorption Studies

This study aims to evaluate the CPs for their effectiveness in removing MB from solutions of the dye. Key factors to be examined include adsorbent loading, contact time, pH effects, initial MB concentration, and adsorption isotherms. Comprehensive kinetic and isotherm analyses will yield mechanistic insights into the adsorption process, while assessments of CP stability will address potential degradation and metal leaching risks.[104]

### *2.3.1. Adsorbent Loading*

Dye loading studies were performed by exposing each CP, at different loadings (shown in Figures S64–S75), to 30 mg $L^{-1}$ of MB solution at pH 6.8 (shown in Figure 7). The CPs displayed a proportional relationship between CP loading and MB adsorption, consistent with trends observed in literature, as would be expected.[105–107] Of the CPs, La-5NIP displayed the highest MB adsorption across the adsorbent loading range between 20 and 100 mg. There is no discernible trend in the data relating to the linkers themselves, which implies that, while they modify the binding characteristics of the metal, they are not determinative of the ability of the CP to uptake MB. Nevertheless, the three top performers are the ones that demonstrated type II $N_2$ adsorption isotherms, and their experimental capacities to adsorb MB match the order of their measured surface areas, that is, La-5NIP (79.9 $m^2$ $g^{-1}$) > Cu-BHA (64.3 $m^2$ $g^{-1}$) > Cu-5NIP (36.9 $m^2$ $g^{-1}$). The poorer performing CPs in this part of the study are those that demonstrated type III $N_2$ adsorption isotherms.

### *2.3.2. Contact Time*

The contact time study describing the MB adsorption kinetics for a given initial dosage of the CP adsorbent provides useful information to understand the extent of an adsorption process.[108] The time factor on MB uptake was evaluated for a 30 mg $L^{-1}$ MB solution at pH 6.8 with a 20 mg CP load (shown in Figures S76–S87). A rapid initial uptake is evident for all CPs except for Cr-BDC and Cr-BHA, which evidence a slower uptake. A strong plateauing effect is noted at 1–8 min, depending on the specific CP, followed by a more gradual uptake of the MB (shown in Figure 8). This is consistent with the notion of the initial high availability of unoccupied active sites on the adsorbent surface. However, as contact time was increased, MB uptake decreased until equilibrium was observed at 60 min, consistent with active site saturation of the CP adsorbent.

### *2.3.3. Effect of pH*

The pH of the dye solution is sometimes a key parameter in the adsorption/dissociation mechanism of dye molecules. This observation is attributed to pH potentially influencing both the adsorbent capacity and adsorbent efficiency as a result of changes at the surface of the adsorbent induced by pH changes.[109,110] The pH of the stock MB solution (30 mg $L^{-1}$) was pH 6.8. The pH of the parent solution was adjusted to pH 3.6 using dilute aqueous HCl and to pH 10.0 using dilute aqueous NaOH. UV–vis spectra of the MB dye/CP mixtures at different pH values (shown in Figures S88–S123) were recorded at 2-min intervals up to 10 min, followed by 10-min intervals up to 1 h (shown in Figure 9). Increasing pH (alkalinity) led to an increase in MB

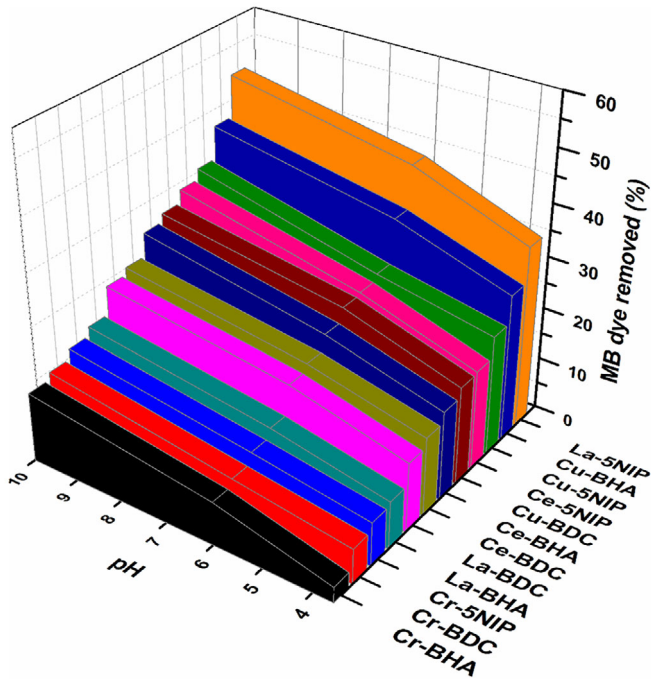


**Figure 9.** The effect of pH on MB adsorption (MB concentration 30 mg $L^{-1}$, time 60 min, CP loading at 20 mg, 298 K).

adsorption for all CPs. Given that the MB molecule is positively charged, the influence of pH could be attributed to increasing negative charge at the surface of the CPs, which would improve ionic attraction between MB and the surface of the CP.[111] Furthermore, the CPs were shown to retain their chemical integrity following regeneration after 24 h of exposure to the various MB solutions, as indicated by the FTIR spectra (shown in Figures S121–S123).

### 2.3.4. Effect of Initial MB Concentration

Dye removal efficiency is dependent on the initial MB concentration.[112] To evaluate the effect of initial MB concentration on the efficiency of removal of the dye, MB solutions of 10, 20, and 30 mg $L^{-1}$ were prepared and exposed to 20 mg of the CP adsorbent (summarized in Table S10). The removal efficiency decreased with increasing MB concentration, consistent with active sites on the CP surfaces becoming saturated as well as equilibrium effects (*cf.* Le Chatelier's principle). The calculated equilibrium adsorption capacity ($q_{exp}$) grows steadily with increasing concentrations, consistent with a non-saturated system at equilibrium.[112,113]

### 2.3.5. Adsorption Kinetics

Pseudo-first-order and pseudo-second-order kinetic modelling was applied to the UV–vis absorbance data (summarized in Table S11 and shown in Figures S127–S150). Pseudo-first-order kinetics assumes that the adsorption rate is proportional to the number of vacant sites on the adsorbent surface, while pseudo-second-order kinetics assumes that the adsorption rate is proportional to the square of the number of vacant sites.[114,115] The coefficient of variation ($R^2$) observed for both the pseudo-first-order model and pseudo-second-order model exhibited good correlation with the experimental data, as shown from the high $R^2$ values for the pseudo-first-order ($0.94 \geq R^2 \geq 0.98$) and for the pseudo-second-order model ($R^2 = 0.99$), which could be indicative of concurrent physisorption and chemisorption processes for MB onto the CPs. The experimental adsorption capacity ($q_{exp.}$) values corresponded more closely to calculated adsorption capacity $q_{e2}$ from the pseudo-second-order model than $q_{e1}$ from the pseudo-first-order model over the MB concentration range ($c_o$) evaluated. The correlation between the $q_{exp}$ values and $q_{e2}$ and the higher $R^2$ values for pseudo-second-order model suggest that the adsorption primarily followed a chemisorption pathway as the adsorption rate-controlling mechanism.[116] It is important to note that both physisorption and chemisorption may occur on the surface of the CP because a layer of dye molecules may be physically adsorbed on top of an underlying chemisorbed layer.[117] The application of the Weber–Morris intra-particle diffusion model to the UV–vis absorbance data (summarized in Table S12 and shown in Figures S151–S162) revealed that the plots obtained ($q_t$ vs. $t_{\frac{1}{2}}$) did not pass through the origin ($C \neq 0$), indicating that the rate-controlling step is not solely governed by intra-particle diffusion but rather that external surface adsorption and intra-particle diffusion contribute to the rate-controlling step.[117]

**Table 6.** PSOM half-life values determined for the CPs.

| CP | $t_{\frac{1}{2}}$ (min) |
|---|---|
| 1) Cr-BHA | 0.17 |
| 2) Cr-BDC | 6.63 |
| 3) Cr-5NIP | 10.06 |
| 4) La-BDC | 14.04 |
| 5) Ce-BHA | 17.86 |
| 6) La-BHA | 19.61 |
| 7) Cu-5NIP | 24.69 |
| 8) Ce-BDC | 25.51 |
| 9) Ce-5NIP | 27.10 |
| 10) Cu-BDC | 27.55 |
| 11) Cu-BHA | 55.87 |
| 12) La-5NIP | 57.08 |

### 2.3.6. Half-Life Adsorption Kinetics

The concept of half-life ($t_{\frac{1}{2}}$) is crucial in assessing the kinetics of adsorption, as it measures the time required for an adsorbent to reduce the initial concentration of a contaminant such as MB by half.[118–120] In this study, the kinetic data for MB adsorption onto the synthesized coordination polymers (CPs) revealed that the adsorption process adhered to second-order kinetics, primarily driven by chemisorption, with $t_{\frac{1}{2}}$ values calculated accordingly (summarized in Table S13). The $t_{\frac{1}{2}}$ values for MB adsorption across the synthesized CPs (summarized in Table 6)

varied significantly, ranging from 0.17 to 57.08 min. For instance, the Cr-BHA CP exhibited the shortest $t_{\frac{1}{2}}$, indicating a rapid adsorption rate, whereas La-5NIP had the longest $t_{\frac{1}{2}}$, reflecting slower kinetics but a higher adsorption capacity. This inverse relationship between $t_{\frac{1}{2}}$ and adsorption capacity suggests that faster adsorbents like Cr-BHA are ideal for quick remediation, while slower but higher-capacity adsorbents like La-5NIP are better suited for long-term dye wastewater treatment. This variation in $t_{\frac{1}{2}}$ provides a useful framework for selecting adsorbents based on the specific kinetic requirements of environmental applications.[121–127]

### 2.3.7. Adsorption Isotherms

The equilibrium data for the removal of MB in the present investigation were assessed using the two-parameter models of Langmuir, Freundlich, and Dubinin–Radushkevich (summarized in Table S14 and shown in Figures S163–S198) and three-parameter models of Redlich–Peterson and Sips equations (summarized in Table S15 and shown in Figures S199–S222). The Langmuir isotherm, which assumes monolayer adsorption, showed an excellent fit to the experimental equilibrium data ($0.95 \leq R^2 \leq 0.99$) for all of the CPs studied, whereby $R_L < 1$ and $q_{max} > 1$ indicated favorable adsorption associated with strong adsorbate-adsorbent interactions. The highest $K_L$ value was observed for Cr-BHA, while the highest $q_{max}$ was observed for La-5NIP by this isotherm model.[128,129] The Freundlich isotherm model, suited to heterogeneous surfaces and multilayer adsorption, displayed a poorer fit compared to the Langmuir model ($0.63 \leq R^2 \leq 0.93$).[130–136] The adsorption intensity index ($1/n$) indicated favorable MB adsorption via chemisorption ($0 < \frac{1}{n} < 1$) for the CPs (except Cr-BHA having $\frac{1}{n} < 0.1$ indicative of a nonlinear irreversible isotherm) and the highest $K_F$ observed for La-5NIP.[137] The Dubinin–Radushkevich isotherm model displayed a good fit to the experimental equilibrium data ($0.92 \leq R^2 \leq 0.99$) for all of the CPs studied with $K_D < 1$ and $E > 8$ kJ mol$^{-1}$, indicative of a microporous adsorbent surface with chemisorption as the primary route for MB uptake by the CPs studied.[138] Furthermore, the saturation capacity ($q_d$) observed agreed with $q_{exp}$ (summarized in Table S10) but was lower than $q_{max}$ by the Langmuir isotherm model.

Although monolayer adsorption appeared more favorable for MB uptake onto the CPs, the $R^2$ value for the Freundlich adsorption isotherms indicated that multilayer MB adsorption onto other CP surfaces may have occurred, that is, pore percolation.[139] To assess the validity of this occurrence, three-parameter hybrid empirical formulas (Redlich–Peterson and Sips models) applicable to both homogeneous and heterogeneous systems and incorporating features of both the Langmuir and Freundlich isotherms were applied to the experimental equilibrium data and the parameters determined (summarized in Table S15).[140,141] The Redlich–Peterson model assumes the presence of both homogeneous and heterogeneous surfaces on the adsorbent, and adsorption does not follow ideal monolayer adsorption.[142] On the other hand, the Sips model is used for heterogeneous monolayer adsorption by an adsorbent with non-uniform adsorption sites and accounts for issues associated with a continual rise in the adsorbed quantity with increased adsorbate concentration in the Freundlich equation.[143] In the Redlich–Peterson model, the value of the constant $\beta$ is a measure of how closely the model conforms to the Langmuir model ($\beta = 1$) or is closer to the Freundlich model ($\beta = 0$). Based on $0 < \beta < 1$ for all of the CPs evaluated, the Redlich–Peterson model indicates a contribution by multiple adsorption modes during MB uptake.[144–146] In the Sips model, the constants $b_s$ and $n$ are related to the energy of adsorption process and the exponential heterogeneity factor, respectively. The Sips equation reduces to Langmuir equation if $n$ is equal to 1, and it implies a homogeneous adsorption process.[147–149] Based on the data obtained, heterogeneous adsorption processes were indicated based on the values obtained for the heterogeneity factor: $0 < n < 1$. Although the Redlich–Peterson displayed a good fit to the experimental equilibrium data ($0.85 \leq R^2 \leq 0.99$), the Sips model showed excellent fit ($0.98 \leq R^2 \leq 0.99$) with a consistently high correlation, whereas the Redlich–Peterson model gave occasional lower $R^2$ values. Thus, the Redlich–Peterson model was deemed less dependable as a descriptive instrument for our investigation.

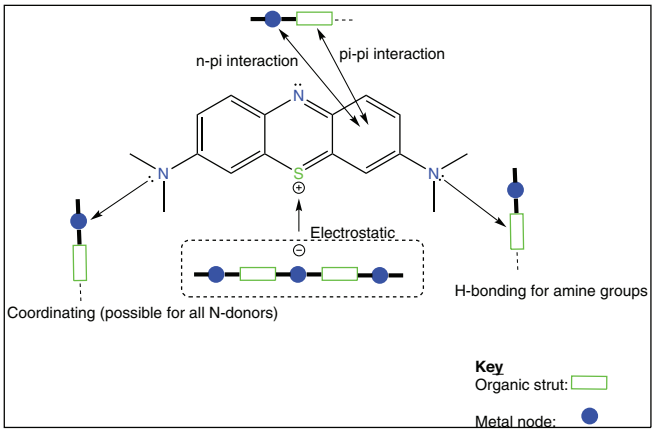


**Figure 10.** MB adsorption onto a generic CP via different interactions.

### 2.3.8. Proposed MB Uptake Mechanism

The adsorption of MB by various adsorbents involves a complex interplay of mechanisms. Multiple interactions between the CPs and the cationic MB dye molecule likely occur simultaneously (shown in Figure 10), with primary adsorbent–adsorbate interactions identified through complementary analytical techniques. For instance, UV–vis spectroscopy reveals n–$\pi$ and $\pi$–$\pi$ stacking interactions by shifts in $\lambda_{max}$ and band positions, while FTIR detects hydrogen bonding, TGA assesses Van der Waals forces, and pH analysis highlights electrostatic interactions. Together with kinetic models and adsorption isotherms, this multifaceted approach provides a comprehensive understanding of adsorption dynamics and underlying mechanisms during MB uptake. Although this study explores key mechanisms for MB adsorption by synthesized CPs, further research is needed to fully unravel the complexities of these interactions.[150,151]

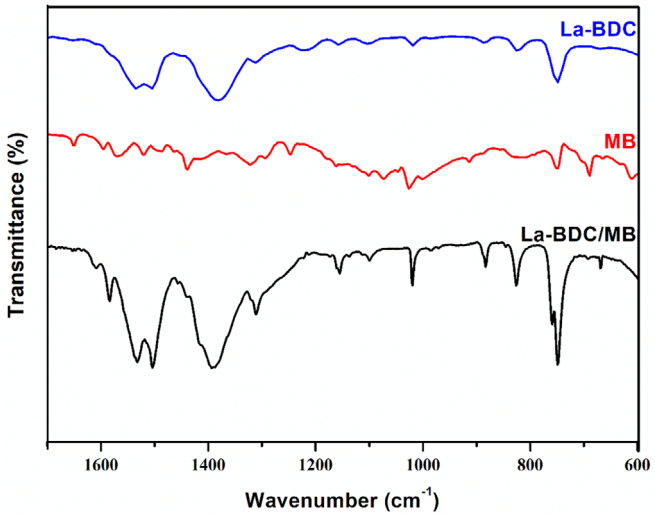


**Figure 11.** Stacked FTIR spectra of La-BDC (blue), MB (red), and La-BDC/MB (black).

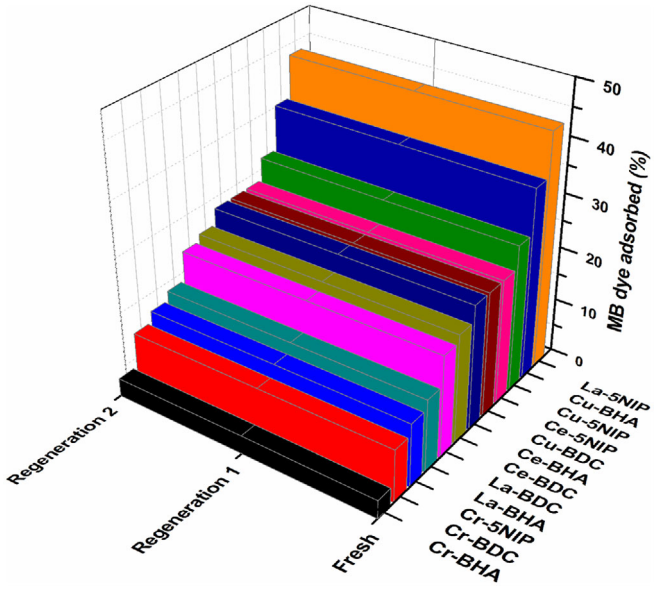


**Figure 12.** Adsorbent reusability for the adsorption of MB onto the respective CPs (pH 6.8, MB concentration of 30 mg $L^{-1}$, time 60 min, CP loading of 20 mg, 298 K).

***Mechanistic insights into MB uptake via adsorption kinetics and isotherms:*** Adsorption kinetics for MB uptake by the CPs showed strong correlation ($R^2$) for both PFOM and PSOM, indicating the involvement of both physisorption and chemisorption. However, PSOM's closer agreement with the experimental adsorption capacity ($q_e$) identified chemisorption as the rate-controlling mechanism. Two-parameter Langmuir and Freundlich isotherms suggested multimodal (monolayer and multilayer) adsorption, while the D–R model confirmed microporosity and chemisorption as the dominant mechanism. The observed multimodal adsorption led to further analysis with three-parameter Redlich–Peterson and Sips models, with the Sips model showing excellent correlation. It revealed heterogeneous surfaces, multiple adsorption site types, and multimodal adsorption, with Cu-BHA favoring physisorption ($n << 1$) and Ce-BDC exhibiting nearly uniform adsorption ($n \approx 1$, indicating equal contributions from physisorption and chemisorption).

***Experimental pH and FTIR analysis toward mechanistic insights into MB uptake:*** pH studies demonstrated increased MB uptake at higher pH levels, likely due to carboxylic group deprotonation (—COOH to —$COO^-$), which increased surface negative charge, enhancing the available MB adsorption sites and promoting electrostatic CP–MB attraction leading to ionic bonding. Stacked FTIR spectra of the CP, MB, and CP/MB systems (e.g., the zoomed region of La-BDC in Figure 11) showed no significant changes in stretching frequencies or peak shifts, further suggesting that physisorption was the dominant process in MB uptake. These experimental findings lay the groundwork for future studies to clarify the exact nature of the CP-MB adsorption interaction.[152–156]

### 2.3.9. CP Reusability

Recovery and reusability of the CPs in the adsorption process was investigated by exposing 20 mg of the respective CP to 30 mg $L^{-1}$ of MB solution at pH 6.8 over 1 h. The CP was recovered after each adsorption experiment by filtration, regenerated by soaking in pure ethanol for 1 h (×3) to remove the guest molecules, and dried before the next MB adsorption cycle, similar to a literature protocol.[157,158] The results evidence comparable MB uptake in each of the three cycles of the materials, without loss of adsorption capacity (shown in Figure 12). The CPs retained their chemical integrity and microcrystallinity following two regeneration cycles as indicated by FTIR and PXRD spectra (shown in Figures S235–S240). For a practical implementation of the method, a cartridge system is likely to work best to enable capture of the dye, which can be readily regenerated by elution of an appropriate solvent, and the solvent would be readily recycled by distillation.

### 2.3.10. CP Leaching

The application of CPs in wastewater treatment faces challenges from metal ion leaching, which is closely linked to their stability in aqueous environments. This leaching poses significant risks to public health and ecosystems by releasing toxic metals, which can bioaccumulate and harm aquatic life.[159–161] Additionally, leaching undermines adsorption efficiency, reusability, and the operational cost-effectiveness of CPs in large-scale operations. This risk is especially pronounced in acidic wastewater conditions where leaching is often accelerated, increasing the contamination potential of these materials and reducing their dye removal efficiency. Consequently, this study investigates the leaching behavior and stability of the high-performing CP candidates studied here, assessing their viability for sustainable wastewater treatment.[162–165] Per the metal leaching percentages (summarized in Table 7) determined via UV–vis spectroscopy (shown in Figures S241–S243), Cu-BHA exhibited low levels of leaching (0.92%) over both 24 and 48 h, indicating relatively robust stability in neutral water. However, when exposed to

**Table 7.** Metal leaching (%) from the selected CPs under varying exposure times and pH.

| CP | 24 h | 48 h | 48 h @ pH 6 | 48 h @ pH 8 |
|---|---|---|---|---|
| Cu-BHA | 0.92 | 0.92 | 1.82 | 0.93 |
| Cu-5NIP | 0.10 | 0.10 | 0.47 | 0.15 |
| La-5NIP | 0.00 | 0.00 | 2.07 | 0.00 |

**Table 8.** $t_{\frac{1}{2}}$ (min) for MB adsorption by various adsorbents.

| Adsorbent | $t_{\frac{1}{2}}$ (min) | Adsorbent | $t_{\frac{1}{2}}$ (min) |
|---|---|---|---|
| 1) Cr-BHA[a)] | 0.17 | 11) $Pb_2$-FSL | 8.26 |
| 2) Pure AC | 0.22 | 12) Clay | 13.90 |
| 3) Seagrass fibers | 0.57 | 13) Algal | 18.90 |
| 4) Palm kernel fiber | 0.75 | 14) Zeolite-NaA | 20.09 |
| 5) UiO-66-$NH_2$ | 1.15 | 15) CP1 | 26.51 |
| 6) Betel nut stalk | 1.27 | 16) CP2 | 40.55 |
| 7) $Zn_2$-FSL | 1.76 | 17) CP3 | 56.41 |
| 8) Rice husk | 3.85 | 18) La-5NIP[a)] | 57.08 |
| 9) Waste apricot AC | 4.00 | 19) DWBC | 100.00 |
| 10) Sepiolite | 5.88 | 20) Natural zeolite | 333.00 |

[a)] CPs reported in this study; FSL: Functionalized salen ligand; $CP_1$: $[Co(BTMDBA)(BIDPE)]_n$; $CP_2$: $[Co(MCBA)(BIMB)\cdot H_2O\cdot OH]_n$; $CP_3$: $[Co_2(\mu\text{-}COO)_2(NC)_2(HIPA)]\cdot 2H_2O)_n$; DWBC: Dehydrated wheat bran carbon.

a mildly acidic environment (pH 6), increased leaching was observed (1.8%), revealing some sensitivity, while a basic environment (pH 8) had minimal effect on leaching compared to the neutral conditions (0.93%). Cu-5NIP also demonstrated high stability, with low leaching (0.10%) in neutral water over 24 and 48 h. Under acidic conditions, leaching from Cu-5NIP increased modestly (0.47%), and a slight increase was observed at pH 8, indicative of low susceptibility to both acidic and basic environments from this CP. La-5NIP showed no detectable leaching in neutral or basic conditions across 24 and 48 h, indicating substantial stability; however, at pH 6, leaching rose markedly to 2.07%, suggesting a pronounced sensitivity to mildly acidic conditions. These observations indicate that while Cu-BHA and Cu-5NIP are robust across a range of pH values, La-5NIP is more suitable for applications in stable or basic pH environments due to its pronounced sensitivity to acidity.

#### *2.3.11. Evaluating MB Adsorptive Performance of the Prepared CPs Versus Reported Adsorbents*

A comparative analysis of the $t_{\frac{1}{2}}$ between the synthesized CPs and various adsorbents from the literature (summarized in Table 8) provided a useful benchmark for evaluating MB adsorption performance.[166–172] While not exhaustive, this comparison highlighted the potential of the CPs in environmental remediation and offered guidance for future material optimization. The physical approach to dye wastewater treatment is promising for large-scale remediation due to its effectiveness and the lack of toxic by-products.

Adsorbents exhibited a range of $t_{\frac{1}{2}}$ values, with Cr-BHA showing the fastest adsorption rate (0.17 min), making it ideal for rapid pollutant removal. Conversely, slower adsorbents like dehydrated wheat bran carbon (100 min) may be more suitable for sustained adsorption, depending on considerations such as capacity. Other materials, such as pure activated carbon (0.22 min) and seagrass fibers (0.57 min), showed rapid kinetics compared to more complex adsorbents like UiO-66$NH_2$ (1.15 min) or rice husk (3.85 min). Longer $t_{\frac{1}{2}}$ values for CP3 (56.41 min) and La-5NIP (57.08 min) are less compelling, potentially suggesting their utility for applications requiring gradual adsorption. These findings underscore the importance of selecting adsorbents based on specific application needs, emphasizing the balance between speed and capacity, and providing a foundation for optimizing future adsorbent materials.

## 3. Experimental Section

### 3.1. Reagents and Materials

All starting materials and reagents are commercially available unless specified. *N*,*N*-dimethylformamide (DMF, 99.8%), nitrate salt hydrates (cerium ($Ce(NO_3)_3\cdot 6\ H_2O$, 99.9%), chromium ($Cr(NO_3)_3\cdot 9H_2O$, 99.9%), copper ($Cu(NO_3)_2\cdot 3H_2O$, 99.9%), lanthanum ($La(NO_3)_3\cdot 6H_2O$, 99.9%) and the organic linkers (benzene-1,4-dicarboxylic acid ($C_8H_6O_4$, 98.0%), 5-nitroisopthalic acid ($C_8H_5NO_6$, 98.0%)) were purchased from Merck Chemicals (Darmstadt, Germany). Benzene-1,4-dihydroxamic acid ($C_8H_8N_2O_4$) was prepared from dimethyl terephthalate ($C_{10}H_{10}O_4$, 99.0%), and hydroxylamine hydrochloride ($NH_2OH\cdot HCl$) was purchased from SRL Chemicals (Maharashtra, India). Methanol, sodium sulphate, and sodium hydroxide were purchased from Rochelle Chemicals (Gauteng, South Africa). All reagents were used without further purification.

### 3.2. Instruments and Methods

The solvothermal synthesis of the CP was run in a bespoke in-house-built thermal bath connected to a magnetic stirrer. Acid-digestive proton nuclear magnetic resonance was performed on a Bruker Ultra-shield 500 MHz NMR spectrometer using minimal addition ($5-10$ drops) of deuterated acetic ($CD_3COOD$), sonicating the mixture until the sample was well dispersed in the acid, followed by the addition of approximately 0.5 mL of deuterated dimethyl sulfoxide (DMSO-$d_6$, calibrated to 2.49 ppm) to dilute and completely dissolve the sample. PXRD was performed on a PANanalytical X-Pert Pro X-ray diffractometer (Almelo, Netherlands) using copper radiation ($\lambda = 1.5406$ Å) with $K_\beta$ filter operated at 40 kV and 40 mA. Single crystal X-ray diffraction was performed on a Bruker Apex DUO equipped with a 4 K CCD diffractometer area detector system equipped with a graphite monochromator and a Mo K$\alpha$ fine-focus sealed tube ($\lambda = 0.71073$ Å operating at 1.35 kW). Thermogravimetric analysis was performed on a Hitachi STA7000 thermoanalyzer (Tokyo, Japan) with a heating rate of 5 °C.min$^{-1}$ under $N_2$ and synthetic air flow (20 mL min$^{-1}$) from room temperature to 800 °C. Scanning electron microscopy with energy dispersive X-ray analysis was performed on a JEM-2100 (Tokyo, Japan); a 200 kV analytical electron microscope equipped with Oxford SDD detector was used to determine the morphology and presence of the metal ion in the

CPs, respectively. $N_2$ adsorption/desorption experiments were conducted with a TriStar 3000 Surface Area coupled to a Flowprep 060 degassing unit (CP samples were heated at 200 °C for several hours under vacuum to remove any gases clinging to the walls of the pores before being exposed to the adsorbate gas ($N_2$) at its condensation temperature (°C) inside the sample chamber at varied pressure and constant temperature). Infrared spectra were recorded using a Shimadzu IRSpirit spectrometer with QATR-S (Tokyo, Japan). Inductively coupled plasma optical emission spectroscopy were recorded on an Thermo iCAP 6500.

### 3.3. Organic Linkers and Coordination Polymers

#### *3.3.1. Synthesis of Ce-BDC (1)*

Cerium nitrate hexahydrate (1.00 g, 2.30 mmol) was dissolved in *N*,*N*-dimethylformamide (15 mL). BDC (0.38 g, 2.30 mmol) was dissolved in *N*,*N*-dimethylformamide (15 mL). The two solutions were introduced to a sealed reactor. The reactor was then heated to 120 °C at a ramp rate of 5 °C $min^{-1}$ and maintained at this temperature for 72 h. The white solid material (1.10 g) formed was then washed under vacuum with (i) DMF (3 × 30 mL) to remove unreacted starting material, followed by (ii) distilled water (3 × 30 mL) and (iii) methanol (3 × 30 mL). The filtered material was then activated by being dried under high vacuum at 100 °C for 12 h prior to characterization. $^1$H NMR (DMSO-$d_6$/$CD_3COOD$, 500 MHz): $\delta$ 11.55 (OH, s, 2H), 8.10 ($H_a$, s, 4H). FTIR ($cm^{-1}$): 1660 (CO asymmetric), 1373 (CO symmetric stretch), 737 (benzene ring C—H bending). The synthetic procedure for the remaining CPs is the same as that for Ce-BDC, differing only in the mass of the respective metal and linker reacted for the desired CP.

#### *3.3.2. Synthesis of Cr-BDC (2)*

Chromium nitrate nonahydrate (1.00 g, 2.5 mmol) was reacted with BDC (0.42 g, 2.5 mmol). $^1$H NMR (DMSO-$d_6$/$CD_3COOD$, 500 MHz): $\delta$ 11.53 (OH, s, 2H), 7.96 ($H_a$, s, 4H). FTIR ($cm^{-1}$): 3372–3218 (OH stretch), 1565 (CO asymmetric), 1379 (CO symmetric stretch), 744 (benzene ring C—H bending).

#### *3.3.3. Synthesis of Cu-BDC (3)*

Copper nitrate trihydrate (1.00 g, 4.1 mmol) was reacted with BDC (0.69 g, 4.1 mmol). $^1$H NMR (DMSO-$d_6$/$CD_3COOD$, 500 MHz): $\delta$ 11.53 (OH, s, 2H), 9.24 ($H_a$, s, 4H). FTIR ($cm^{-1}$): 3235 (OH stretch), 1581 (CO asymmetric), 1392 (CO symmetric stretch), 744 (benzene ring C—H bending).

#### *3.3.4. Synthesis of La-BDC (4)*

Lanthanum nitrate hexahydrate (1.00 g, 2.3 mmol) was reacted with BDC (0.43 g, 2.3 mmol). $^1$H NMR (DMSO-$d_6$/$CD_3COOD$, 500 MHz): $\delta$ 11.54 (OH, s, 2H), 7.80 ($H_a$, s, 4H). FTIR ($cm^{-1}$): 2924–3021 (OH stretch), 1581 (CO asymmetric), 1379 (CO symmetric stretch), 744 (benzene ring C—H bending).

#### *3.3.5. Benzene-1,4-dihydroxamic Acid (BHA)*

Hydroxylamine hydrochloride (3.20 g, 45 mmol) was mixed with sodium hydroxide (3.60 g, 90 mmol) and sodium sulfate (0.60 g, 4 mmol) in deionized water (45 mL) and added to dimethyl terephthalate (3.00 g, 30 mmol) dissolved in methanol (50 mL), followed by stirring for 72 h at 40 °C. The reaction solution was acidified to pH 5.5 using 5% HCl, and the solvent was removed in vacuo, yielding a yellow solid. Methanol (60 mL) was added, and sodium chloride was filtered off, followed by solvent removal in vacuo to yield a white solid, which was recrystallized in hot water to form BHA. Yield: 2.03 g, 10.45 mmol, 35%.$^1$H NMR (DMSO-$d_6$/$CD_3COOD$, 500 MHz): $\delta$ 12.00 (NH, b), 9.74 (OH, s, 2H), 7.90 ($H_a$, s, 4H). FTIR ($cm^{-1}$): 3285 (NH), 2721 (OH), 1645 (C═O), 1605 (CO), 1562 (CN), 1543 (C—C aromatic stretch). E.A. Anal. (%) calculated for BHA C: 48.98; H: 4.11; N: 14.28 and found C: 49.30; H: 4.18; N: 14.50.

#### *3.3.6. Synthesis of Ce-BHA (5)*

Cerium nitrate hexahydrate (1.00 g, 2.30 mmol) was reacted with BHA (0.44 g, 2.30 mmol). $^1$H NMR (DMSO-$d_6$/$CD_3COOD$, 500 MHz): $\delta$ 11.55 (NH, b), 9.73 (OH, s, 2H), 7.85 ($H_a$, s, 4H). FTIR ($cm^{-1}$): 1543 (N—O stretch), 1380 (C—O stretch).

#### *3.3.7 Synthesis of Cr-BHA (6)*

Chromium nitrate nonahydrate (1.00 g, 2.5 mmol) was reacted with BHA (0.50 g, 2.5 mmol). FTIR ($cm^{-1}$): 3373 (OH stretch), 1645 (N—O stretch), 1386 (C—O stretch).

#### *3.3.7. Synthesis of Cu-BHA (7)*

Copper nitrate trihydrate (1.00 g, 4.1 mmol) was reacted with BHA (0.80 g, 4.1 mmol). $^1$H NMR (DMSO-$d_6$/$CD_3COOD$, 500 MHz): $\delta$ 11.55 (NH, b), 9.74 (OH, s, 2H), 7.85 ($H_a$, s, 4H). FTIR ($cm^{-1}$): 3373 (OH stretch), 1658 (NH bending), 1522 (NO stretch), 1381 (C—O stretch).

#### *3.3.8. Synthesis of La-BHA (8)*

Lanthanum nitrate hexahydrate (1.00 g, 2.3 mmol) was reacted with BHA (0.40 g, 2.3 mmol). $^1$H NMR (DMSO-$d_6$/$CD_3COOD$, 500 MHz): $\delta$ 11.60 (NH, b), 9.74 (OH, s, 2H), 7.86 ($H_a$, s, 4H). FTIR ($cm^{-1}$): 3259 (OH stretch), 1555 (N—O stretch), 1385 (C—O stretch).

#### *3.3.9. Synthesis of Ce-5NIP (9)*

Cerium nitrate hexahydrate (1.00 g, 2.30 mmol) was reacted with 5NIP (50 g, 2.30 mmol). $^1$H NMR (DMSO-$d_6$/$CD_3COOD$, 500 MHz): $\delta$ 11.00 (OH, b, 2H), 8.87 ($H_b$, s, 1H), 8.82 ($H_a$, s, 2H). FTIR ($cm^{-1}$): 3113 (OH stretch), 1521 (CO asymmetric), 1420 (CO symmetric).

#### *3.3.10. Synthesis of Cr-5NIP (10)*

Chromium nitrate nonahydrate (1.00 g, 2.5 mmol) was reacted with 5NIP (0.50 g, 2.5 mmol). FTIR ($cm^{-1}$): 2998–3581 (OH stretch), 1530 (CO asymmetric), 1420 (CO symmetric).

#### *3.3.11. Synthesis of Cu-5NIP (11)*

Copper nitrate trihydrate (1.00 g, 4.1 mmol) was reacted with 5NIP (0.90 g, 4.1 mmol). $^1$H NMR (DMSO-$d_6$/$CD_3COOD$, 500 MHz): $\delta$ 10.99 (OH, b, 2H), 8.63 ($H_b$, s, 1H), 8.62 ($H_a$, s, 2H). FTIR ($cm^{-1}$): 3563 (OH stretch), 1521 (CO asymmetric), 1420 (CO symmetric).

**Table 9.** Overview of typical BET constant (*C*) value ranges categorized by adsorbate–adsorbent interaction strength with examples.

| *C*-Value | Adsorbent–Adsorbate Interaction | Example |
|---|---|---|
| $1 \leq C < 50$ | Weak | Non-polar gases on non-polar surfaces (London dispersion force) |
| $50 \leq C < 500$ | Moderate | Gas-solid systems at room temperature |
| $C \geq 500$ | Strong | Gases on highly porous adsorbent surfaces (Van der Waals force) |

#### 3.3.12. Synthesis of La-5NIP (12)

Lanthanum nitrate hexahydrate (1.00 g, 2.3 mmol) was reacted with 5NIP (0.50 g, 2.3 mmol). $^1$H NMR (DMSO-$d_6$/$CD_3COOD$, 500 MHz): $\delta$ 10.96 (OH, b, 2H), 8.73 ($H_a$, s, 2H), 8.71 ($H_b$, s, 1H). FTIR ($cm^{-1}$): 3545 (OH stretch), 1560 (CO asymmetric), 1398 (CO symmetric).

### 3.4. Gas Sorption Studies

#### 3.4.1. BET Theory

Brunauer–Emmett–Teller (BET) theory describes a mathematical Equation (2) to calculate the specific surface area and pore size distribution from the volume of the probing gas (adsorbate) adsorbed to the surface of the particles (including pores) from the known size of the adsorbate gas molecule.[173]

$$\frac{P}{V\,(P_o - P)} = \frac{1}{V_m C} + \left(\frac{C-1}{V_m C}\right)\frac{P}{P_o} \tag{2}$$

where $P$ is equilibrium pressure of adsorbate, $P_o$ is the saturation pressure of adsorbate, $V$ is adsorbed gas quantity, $V_m$ is the adsorbed gas quantity to form a saturated monolayer per gram of adsorbent, and $C$ is the dimensionless constant related to the enthalpy of adsorbate adsorption.

The magnitude of $C$, the BET constant, is calculated using Equation (3) and measures the strength of the adsorbent–adsorbate interaction (summarized in Table 9).[174]

$$C = \frac{(e^{(E_1)} - e^{(E_L)})}{RT} \tag{3}$$

where $E_1$ and $E_L$ are the heat of adsorption for the first and subsequent layers, respectively; $R$ is the universal gas constant, and $T$ is the absolute temperature.

The applicability of Equation (3) relies on several key assumptions, that is, (a) multilayered adsorption must occur; (b) the heat of adsorption for the first layer differs from that of subsequent layers ($E_1 \neq E_L$); (c) molecules adsorbed within the same layer do not interact laterally; (d) the adsorbent surface is homogeneous with equivalent adsorption sites; (e) adsorption only occurs once at a specific site; (f) each adsorbed layer is in equilibrium with the adsorbate gas phase; and (g) each adsorbed layer obeys the Langmuir adsorption isotherm. The adsorption behavior of materials at constant temperature typically conform to one of six IUPAC-classified adsorption isotherms (shown in Figure S28).[175–178]

**Table 10.** Overview of the shape, adsorbate–adsorbent interaction, and pore structure associated with the four hysteresis loops of adsorption isotherms as classified by IUPAC.

| Type | Hysteresis Loop | Pore Structure |
|---|---|---|
| H1 | Narrow | Cylindrical (open at both ends) |
| H2 | Broad | Ink bottle (neck-like with wide body) |
| H3 | Steep desorption branch | Groove (macroporous) |
| H4 | Parallel and horizontal branches | Slit (microporous) |

Per the assumptions (a–g) required for BET theory to be satisfied, Equation (3) is only applicable to materials displaying type II (reversible isotherm for nonporous or macroporous materials) or type IV (reversible isotherm for mesoporous materials) isotherms. The remaining isotherms (types I, III, V, and VI) are excluded, as these isotherms do not conform to the key assumptions outlined above, that is; type I isotherms represent monolayer adsorption, type III isotherms provide no information about monolayer coverage, type V isotherms display hysteresis without multilayer adsorption, while type VI isotherms exhibit distinct stepwise adsorption stages characteristic of materials having highly uniform nonporous surfaces.[179] In addition, IUPAC classification also defines four types of hysteresis loops (shown in Figure S29) observed in isotherms (types IV and V) of porous materials possessing complex adsorption/desorption behaviors attributed to pore structure (summarized in Table 10).[180]

#### 3.4.2. BJH Theory

Barrett, Joyner, and Halenda (BJH) theory is primarily used to calculate the pore size distribution of mesoporous materials via analysis of the gas desorbed as a function of the relative pressure. The BJH method is based on the Kelvin equation (Equation (5)) to determine pore size (microporous: < 2, mesoporous: 2–50, or macroporous: > 50) by relating the pressure of the adsorbed gas to the curvature of the liquid meniscus inside the pores and predict capillary condensation. However, pore size determination of complex materials may be challenging, as Equation (4) neglects interactions beyond surface tension and assumes that the pores are cylindrically shaped.[181–184]

$$\ln\left(\frac{P}{P_o}\right) = \frac{2\gamma V_m}{r\mathrm{RT}} \tag{4}$$

where $P$ is the equilibrium vapor pressure inside the pore, $P_o$ is the saturation vapor pressure of the bulk liquid, $\gamma$ is the surface tension of the liquid, $V_m$ is the molar volume of the liquid, $R$ is the universal gas constant, $T$ is the absolute temperature, and $r$ is the radius of curvature of the meniscus.

#### 3.4.3. t-Plot Theory

The thickness-plot (*t*-plot) method, developed by De Boer et al., is a graphical technique used in gas sorption analysis to determine the surface area and pore volume of porous materials, particularly those that display non-BET compliant isotherms. This method compares the adsorption isotherm of the material being studied with a reference adsorption isotherm of a nonporous material (ideal isotherm curve) having a similar surface chemistry to ascertain the thickness of the adsorbed layer on the experimental material surface as a function of relative pressure ($\frac{P}{P_o}$). Using this approach, an adsorp-

tion isotherm $N^{o}_{ads}(P)$ of a given gas on a flat surface having a specific surface area ($S$) with density ($\rho_0$) can be converted into the average thickness $t(P)$ of the adsorbed film on the surface via Equation (5) to produce a $t$-curve.[185,186]

$$t(P) = \frac{N^{o}_{(ads)}(P)}{p_o S} \tag{5}$$

where $N^{o}_{ads}$(P) is the adsorption isotherm on a flat surface with specific surface area (mol/g), $\rho_o$ is the pressure (adsorbed phase density = liquid density) (mol/m$^3$), and $S$ is the specific surface area (m$^2$/g).

A $t$-plot is generated by converting $t(P)$ (Equation (5)) into the volume of adsorbate adsorbed ($V_{ads}$) using Equation (6) and plotting it against the statistical thickness ($t$) to identify different porosity regions of the experimental material.

$$t\,(P) = 1 - \sqrt{\frac{1 - \left(\frac{P}{P_o}\right)V_{ads}}{V_o}} \tag{6}$$

where $V_{ads}$ is the volume of adsorbate adsorbed at a given pressure and $V_o$ is the maximum volume of adsorbate adsorbed.

If the $t$-plot is initially linear, it could indicate micropore filling and suggests that the material displays an identical adsorption behavior as the flat reference surface for that specific pressure range ($t$-plot gradient = external surface area of the material). In contrast, any departure from the linearity at higher values of $t$ is indicative of a mesoporous region, whereby condensation (steep gradient) or adsorption on the pore walls (gentle gradient) may be observed. Since the $t$-plot method compares the isotherm and an ideal adsorption curve, it is necessary to ensure that the selected model closely describes the layer of adsorbate thickness on the adsorbent surface since no universal thickness curve exists. In addition, the $t$-plot method has been proven to be accurate for microporous surfaces where the adsorbed layer thickness is dependent on pore diameter and less accurate for mesoporous materials where the adsorbed layer thickness is independent of pore diameter.[103]

Per $t$-plot theory, the micropore volume and surface area of the CPs were determined utilizing the Harkins–Jura (H–J) statistical thickness equation (Equation (7)) adapted from Equation (6) to estimate the thickness of the adsorbed film.[98]

$$t = \left[\frac{13.99}{(0.034 - \log_{10}\left(\frac{P}{P_o}\right)}\right]^{\frac{1}{2}} \tag{7}$$

where $t$ is the adsorbed layer thickness, $P$ is the adsorbate equilibrium pressure, and $P_o$ is the adsorbate saturation vapor pressure.

Assumptions: (i) Surface area correction factor: 1.0. (ii) Density conversion factor: 1.5 × 10$^{-3}$. and (iii) Thickness range: 3.5–5.0 Å.

### 3.5. Dye Adsorption

A 1 M stock solution of methylene blue was prepared using deionized water. The effect of several factors on MB adsorption, such as the pH, CP loading, and contact time, was investigated using the one-factor-at-a-time method in the dark to minimize potential photodegradation. The adsorption process was followed by ultraviolet–visible spectroscopy (UV–vis; Hellma Analytics quartz cuvette at constant room temperature on a Shimadzu UV-1800 spectrophotometer). The stock MB solution was diluted to a concentration of 30 mg L$^{-1}$, which corresponded to an absorbance (Abs) of approximately 1 (MB; $\lambda_{abs}$ 664 nm), ensuring optimal sensitivity and accurate quantification using UV–vis spectroscopy. The CP adsorbent mass was set at 20 mg, optimized for use in standard 1 cm path length cuvettes, providing sufficient surface area for efficient adsorption while fitting within the experimental constraints. To further investigate the effect of adsorbent loading on MB uptake, additional studies were conducted using CP masses of 40, 60, 80, and 100 mg. These incremental studies confirmed the suitability of the 20 mg baseline and provided insights into the scalability of the CPs adsorption capacity. The MB sorption efficiency (%) and equilibrium adsorption capacity were calculated by Equations (8) and (9), respectively.[82]

$$\text{DyeRemoval}\,(\%) = \frac{c_o - c_f}{C_o} \times 100 \tag{8}$$

where $c_o$ is the initial feed concentration of dye solution and $c_f$ is the final concentration of dye solution after adsorption.

$$Q_e = \left[\frac{(c_o - c_e) \times V}{M}\right] \tag{9}$$

where $Q_e$ is the equilibrium adsorption capacity (mg g$^{-1}$), $c_e$ is the equilibrium concentration of MB (mg L$^{-1}$), $V$ is the MB solution volume (L), and $M$ is the adsorbent mass (g).

### 3.6. Kinetics, Isotherm, and Statistics

#### *3.6.1. Adsorption Kinetic Models*

Adsorption kinetics studied the adsorbent–adsorbate reaction rate. As adsorption and desorption are time-dependent processes, their kinetic parameters portrayed the movement of the adsorbate within and onto the surface sites of the adsorbent. In this study, the adsorption data were fitted by pseudo-first-order, pseudo-second-order, and intraparticle diffusion kinetic models.[187] The most effective model was selected to describe the adsorbent-adsorbate interaction between MB and the CPs based on (i) consistency between the experimental and the theoretical values of the model and (ii) the coefficient of determination value ($R^2$) being close to or equal to 1 from the statistical function of the Origin Pro 8.5 software.[188]

***a) Pseudo-first-order kinetic model:*** The pseudo-first-order model described by Equation (10) assumes that the rate of change is directly proportional to the difference in saturation concentration and the amount of MB dye uptake with time, whereby the reaction rate is governed by physisorption.[189]

$$\ln(q_e - q_t) = \ln q_e - k_1 t \tag{10}$$

where $k_1$ is the first-order adsorption rate constant (min$^{-1}$), $t$ is time (min), $q_e$is the equilibrium adsorption capacity (mg g$^{-1}$), and $q_t$ is the equilibrium adsorption capacity at various times $t$ (mg g$^{-1}$).

***b) Pseudo-second-order kinetic model:*** The pseudo-second-order model described by Equation (11) assumes MB dye uptake decreases linearly as the adsorption rate increases, whereby the reaction rate is governed by chemisorption.[190]

$$\frac{t}{q_t} = \frac{1}{K_2 q_e^2} + \frac{t}{q_e} \tag{11}$$

where $k_2$ is the second-order adsorption rate constant (g $mg^{-1}$ $min^{-1}$), $t$ is time (min), $q_e$is the equilibrium adsorption capacity (mg $g^{-1}$), and $q_t$ is the equilibrium adsorption capacity at various times $t$ (mg $g^{-1}$).

***c) Weber–Morris intra-particle diffusion model:*** The intraparticle diffusion model can be described by Equation (12). According to Equation (12), the linear plot of $t^{\frac{1}{2}}$ versus $q_t$ passes through the origin (C=0) when intra-particle diffusion is the only rate-controlling step. However, when the linear plot of $t^{\frac{1}{2}}$ versus $q_t$ does not pass through the origin ($C \neq 0$), both surface adsorption and intra-particle diffusion participate in the rate-controlling step.[191]

$$q_t = k_{ip}t^{1/2} + c \tag{12}$$

where $k_{ip}$ is intra-particle diffusion rate constant for adsorption (mg $g^{-1}$ $min^{-1/2}$) and $c$ is the intercept representing boundary layer thickness (mg $g^{-1}$).

### 3.6.2. Adsorption Isotherm Models

The adsorption process is divided into two parts: adsorbent adsorption and desorption from the adsorbent. When the rate of the two processes is the same, the adsorption will enter a dynamic equilibrium state at constant pH and temperature. Adsorption isotherms are used to study the relationship between the equilibrium adsorption capacity and the equilibrium concentration of pollutants under certain conditions (temperature and pH remain unchanged). The adsorption isotherms were studied to provide a basis for revealing adsorption behavior, indicating possible adsorption mechanism and estimating adsorption capacity. In this study, the Langmuir and Freundlich models were used to describe the isothermal adsorption behavior of the respective CPs.

***a) Langmuir model:*** The Langmuir model assumes (i) adsorption is localized on a monolayer, (ii) each molecule possesses constant enthalpies and sorption activation energy, and (iii) the adsorbent adsorption sites are homogeneous, possessing the same adsorption capacity. The Langmuir isotherm equation can be described by Equation (13), and its shape can be calculated from the separation factor $R_L$ using Equation (14), whereby $R_L = 1$ (linear isotherm), $R_L = 0$ (irreversible isotherm), $0 < R_L < 1$ (favorable isotherm), or $R_L > 1$ (unfavorable isotherm).[192]

$$\frac{c_e}{q_e} = \frac{1}{q_{max}K_L} + \frac{c_e}{q_{max}} \tag{13}$$

where $c_e$ is the equilibrium aqueous-phase concentration of adsorbate (mg $L^{-1}$), $q_e$ is the equilibrium adsorbent-phase concentration of adsorbate (mg $g^{-1}$), $q_{max}$ is the maximum monolayer coverage capacity (mg $g^{-1}$), and $K_L$ is the Langmuir constant (L $mg^{-1}$).

$$R_L = \frac{1}{1 + K_L C_i} \tag{14}$$

where $c_i$is the initial MB dye concentration (mg $L^{-1}$) and $K_L$ is the Langmuir constant (L $mg^{-1}$).

***b) Freundlich model:*** The Freundlich model describes non-ideal reversible multilayer adsorption over a heterogeneous surface and is described by Equation (15).[192] $K_F$ and $\frac{1}{n}$ are empirical constants characteristic of the system, whereby $K_F$ is the adsorption coefficient representing the relative adsorption capacity of the adsorbent and $\frac{1}{n}$ represents the adsorption intensity of adsorbate onto the adsorbent (surface heterogeneity). When $\frac{1}{n} < 0.1$, the surface of the adsorbent becomes more heterogeneous with the adsorption approaching a nonlinear irreversible isotherm; $0 < \frac{1}{n} < 1$ indicates favorable adsorption via a chemisorption process while $\frac{1}{n} > 1$ indicates unfavorable adsorption isotherms occurring via a cooperative process.[193]

$$\ln Q_e = \ln K_f + \frac{1}{n}\ln c_e \tag{15}$$

where $c_e$is the equilibrium aqueous-phase concentration of adsorbate (mg $L^{-1}$), $q_e$is the equilibrium adsorbent-phase concentration of adsorbate (mg $g^{-1}$), $n$ is adsorption intensity, and $K_f$ is the Freundlich constant (mg $g^{-1}$).

***c) Dubinin–Radushkevich model:*** The temperature-dependent Dubinin–Radushkevich model is a semi-empirical equation only suitable for an intermediate range of adsorbate concentrations in which adsorption follows a pore-filling mechanism.[194–197] The Dubinin–Radushkevich equation was developed as an adaptation of the Polanyi potential theory of adsorption shown by Equation (16) to describe the adsorption of gases onto solids by assuming that the distribution of pores in adsorbents obeys Gaussian energy distribution as shown in Equation (17) to estimate the average free energy of adsorption (kJ $mol^{-1}$) using Equation (18).[198,199]

$$\varepsilon = \mathrm{RTln}(1 + \frac{1}{C_e}) \tag{16}$$

where $R$ is the universal gas constant (8.314 J $mol^{-1}$ $K^{-1}$), $T$ is the Kelvin temperature (K), and $c_e$ is the equilibrium aqueous-phase concentration of adsorbate (mg $L^{-1}$).

$$\ln q_e = \ln q_d - K\varepsilon^2 \tag{17}$$

where $q_e$is the equilibrium adsorbent-phase concentration of adsorbate (mg $g^{-1}$), $q_d$ is the theoretical saturation capacity (mg $g^{-1}$), $K$ is the activity coefficient ($mol^2$ $kJ^{-2}$), and $\varepsilon$ is the Polanyi potential (kJ $mol^{-1}$).

$$E = 1/\sqrt{2K} \tag{18}$$

where $E$ is the mean adsorption energy (kJ $mol^{-1}$).

***d) Redlich–Peterson isotherm model:*** The Redlich–Peterson isotherm is an empirical isotherm incorporating a mix of the Langmuir and Freundlich isotherms so that the mechanism of adsorption is a mix and does not follow ideal monolayer adsorption. At low concentrations, the model approaches the Langmuir isotherm ($\beta \sim 1$), and at high concentrations, it approaches the Freundlich isotherm ($\beta \sim 0$). The linear form of the Redlich–Peterson isotherm is shown in Equation (19).[200,201]

$$\ln\frac{c_e}{q_e} = \beta \ln c_e - \ln K_r \tag{19}$$

where $c_e$ is the equilibrium aqueous-phase concentration of adsorbate (mg $L^{-1}$), $q_e$ is the equilibrium adsorbent-phase concentration of adsorbate (mg $g^{-1}$), $\beta$ is the exponent that lies between 0 and 1, and $K_r$ is the Redlich–Peterson isotherm constant (L $g^{-1}$).

***e) Sips isotherm model:*** The Sips isotherm is derived from the limiting behavior of the Langmuir and Freundlich isotherms and is valid for localized adsorption without adsorbate-adsorbate interactions, whereby the isotherm reduces to Freundlich when $c_e$ approaches

a low value and displays Langmuir monolayer sorption characteristics at high $c_e$ values.[140,192] The linear Sips equation is shown in Equation (20).[202,203]

$$\ln\left(\frac{q_e}{q_m - q_e}\right) = \frac{1}{n}\ln(c_e) + \ln(b_s)^{\frac{1}{2}} \quad (20)$$

where $q_e$ is the equilibrium adsorbent-phase concentration of adsorbate (mg $g^{-1}$), $q_m$ is the maximum monolayer adsorption capacity (mg $g^{-1}$), $c_e$ is the equilibrium aqueous-phase concentration of adsorbate (mg $L^{-1}$), $b_s$ is the Sips isotherm constant related to energy of adsorption, and $n$ is the exponential heterogeneity factor.

### 3.7. Reusability of CPs

CP reusability, an important criterion for a CP in the adsorption process, was assessed using ethanol (EtOH) as the desorbing agent.[204] Following the first MB adsorption cycle, the respective CP was filtered off from the MB solution, soaked in pure EtOH for 1 h, and filtered from the EtOH solution. The CP was soaked three times in EtOH before being dried in an oven at 110 °C for 24 h before being used for the next MB adsorption cycle.

### 3.8. CP Leaching

The stability of the three CPs with the highest MB adsorption efficiency (Cu-5NIP, Cu-BHA, and La-5NIP) was assessed over 48 h by measuring metal ion leaching using UV–vis spectroscopy. Each CP (20 mg) was immersed in 4 mL of distilled water (pH 7) at room temperature to simulate realistic environmental conditions, as this pH represented the midpoint of the optimal range (pH 6–8) for MB adsorption. Aliquots were filtered and analyzed over 48 h at 24-h intervals to detect metal ions released into the solution. This procedure was repeated for solutions adjusted to pH 6 (using HCl) and pH 8 (using NaOH) after 48 h to evaluate stability across the optimal pH spectrum for MB adsorption. Distilled water served as the control throughout the experiment. Additionally, solutions of the corresponding metal salts, $Cu(NO_3)_2{\cdot}3H_2O$ (29.4 mM; $\lambda_{abs}$ 300 nm) and $La(NO_3)_3{\cdot}6H_2O$ (25.2 mM; $\lambda_{abs}$ 300 nm), were prepared to achieve an absorbance of 1, allowing for direct quantification of leached metal ions (%).

## 4. Conclusion

In this study, a range of CPs were synthesized and characterized by combining BDC, BHA, and 5NIP linkers with Ce, Cr, Cu, and La. Surface area and porosity analyses via BET, BJH, and *t*-plot models revealed significant structural insights. The BET model showed type II adsorption isotherms for Cu-5NIP, Cu-BHA, and La-5NIP with surface areas ranked as La-5NIP > Cu-BHA > Cu-5NIP, while pore diameters followed the order Cu-5NIP > Cu-BHA > La-5NIP, indicating mesoporosity. Other CPs exhibited type III isotherms, precluding accurate BET surface area determination. BJH analysis confirmed uniform surface properties, and *t*-plot data suggested uniform mesoporosity with multilayer adsorption characteristics. Overall, these findings underscored the mesoporous nature of the CPs. The CPs displayed distinct adsorption kinetics for MB, following pseudo-second-order kinetics primarily driven by chemisorption. MB uptake was influenced by external surface adsorption and intra-particle diffusion, with La-5NIP showing the highest MB adsorption, followed by Cu-BHA and Cu-5NIP. Optimal MB adsorption was observed under basic conditions, with rapid initial adsorption within 10 min and equilibrium achieved by 60 min. Isotherm studies indicated strong adsorbate–adsorbent interactions with La-5NIP showing the highest adsorption capacity and affinity for MB as reflected in both the Langmuir and Freundlich models. The Sips isotherm best described the adsorption behavior, indicating heterogeneous surface interactions and a dual mechanism of physisorption and chemisorption, which emphasized the material's suitability for complex contaminant adsorption. The study also highlighted CP stability under various pH conditions whereby Cu-BHA and Cu-5NIP showed minimal leaching in neutral and basic environments, though mild acidic exposure increased leaching, particularly for La-5NIP, indicating a greater suitability for this particular CP in stable or basic conditions. Comparatively, the CPs exhibited competitive $t_{\frac{1}{2}}$ values with existing adsorbents, suggesting both rapid and gradual adsorption options depending on application needs. The CPs demonstrated reusability over three cycles (fresh plus two repeats), with Cu-BHA showing minimal leaching even after 48 h of exposure to distilled water. Collectively, these results underscore the CPs adaptability, reusability, and dual-mode adsorption mechanisms, which present these materials as valuable alternatives in scalable dye capture wastewater applications.

## Author Contributions

**Cresten Moodley**: Conceptualization; methodology; software; validation; formal analysis. **Kaushik Mallick**: Supervision; visualization; writing—review and editing. **Alfred Muller**: Supervision; resources; conceptualization; methodology; software. **D. Bradley G. Williams**: Supervision; data curation; writing—review and editing.

## Acknowledgements

The authors would like to thank the National Research Foundation (reference MND200413512950) for their financial support and the Department of Chemical Sciences at the University of Johannesburg for the availability of instrumentation to make this project a viable study.

## Conflict of Interests

The authors declare no conflict of interest.

## Data Availability Statement

The data that support the findings of this study are available in the Supporting Information of this article.

**Keywords:** Adsorbent · Adsorption · Coordination polymer · Methylene blue · Solvothermal

[1] H. Maleki, N. Hüsing, *Appl. Catal. B Environ.* **2018**, *221*, 530–555.
[2] F. H. Saboor, N. Nasirpour, S. Shahsavari, H. Kazemian, *Chem. Asian J.* **2022**, *17*, e202101105.
[3] J. Huang, X. Gao, M. Wang, Z. Yang, L. Xiang, Y. Li, J. Ning, *J. Gastrointest. Surg.* **2023**, *27*, 1837–1845.
[4] P. O. Oladoye, T. O. Ajiboye, E. O. Omotola, O. J. Oyewola, *Results Eng.* **2022**, *16*, 100678.
[5] A. Seitkazina, J. K. Yang, S. Kim, *Precision and Future Medicine* **2022**, *6*, 193–208.
[6] I. Khan, K. Saeed, I. Zekker, B. Zhang, A. H. Hendi, A. Ahmad, I. Khan, *Water* **2022**, *14*, 242.
[7] P. Sharma, A. F. Olufemi, K. Qanungo, *Mater. Today Proc.* **2022**, *49*, 1556–1565.
[8] J. Pomicpic, G. C. Dancel, P. J. Cabalar, J. Madrid, *Radiat. Phys. Chem.* **2020**, *172*, 108737.
[9] M. Contreras, C. D. Grande-Tovar, W. Vallejo, C. Chaves-López, *Water* **2019**, *11*, 282.
[10] M. Rafatullah, O. Sulaiman, R. Hashim, A. Ahmad, *J. Hazard. Mater.* **2010**, *177*, 70–80.
[11] V. Katheresan, J. Kansedo, S. L. Lau, *J. Environ. Chem. Eng.* **2018**, *6*, 4676–4697.
[12] J. Fito, M. Abewaa, A. Mengistu, K. Angassa, A. D. Ambaye, W. Moyo, T. Nkambule, *Sci. Rep.* **2023**, *13*, 5427.
[13] A. M. Aibinu, T. A. Folorunso, A. A. Saka, L. A. Ogunfowora, K. O. Iwuozor, J. O. Ighalo, *Reg. Stud. Mar. Sci.* **2022**, *52*, 102308.
[14] J. Liu, N. Wang, H. Zhang, J. Baeyens, *J. Environ. Manag.* **2019**, *238*, 473–483.
[15] C. Yang, L. Li, J. Shi, C. Long, A. Li, *J. Hazard. Mater.* **2015**, *284*, 50–57.
[16] M. T. Yagub, T. K. Sen, S. Afroze, H. M. Ang, *Adv. Coll. Int. Sci.* **2014**, *209*, 172–184.
[17] V. K. Gupta, R. Kumar, A. Nayak, T. A. Saleh, M. Barakat, *Adv. Coll. Int. Sci.* **2013**, *193*, 24–34.
[18] S. H. Huo, X. P. Yan, *J. Mater. Chem.* **2012**, *22*, 7449–7455.
[19] J. Liu, J. T. Culp, S. Natesakhawat, B. C. Bockrath, B. Zande, B. C. Sankar, G. Garberoglio, J. K. Johnson, *J. Phys. Chem. C* **2007**, *111*, 9305–9313.
[20] K. C. Padmanabhan, A. Joseph, X. Y. Thirumurugan, T. J. Huang, J. L. Emge, *Inorganica Chim. Acta* **2007**, *360*, 2583–2588.
[21] N. Manousi, D. A. Giannakoudakis, E. Rosenberg, G. A. Zachariadis, *Molecules* **2019**, *24*, 4605.
[22] G. W. Kajjumba, M. Attene-Ramos, E. J. Marti, *Sci. Total Environ.* **2021**, *800*, 149556.
[23] I. Blinova, M. Muna, M. Heinlaan, A. Lukjanova, A. Kahru, *Nanomater* **2020**, *10*, 328.
[24] J. O. Ighalo, F. O. Omoarukhe, V. E. Ojukwu, K. O. Iwuozor, C. A. Igwegbe, *Cleaner Chem. Eng.* **2022**, *3*, 100042.
[25] A. C. Fingolo, B. C. Klein, M. C. Rezende, C. A. Silva e Souza, J. Yuan, G. Yin, M. Strauss, *Waste Biomass Valori.* **2020**, *11*, 1–13.
[26] D. Chakraborty, A. Yurdusen, G. Mouchaham, F. Nouar, C. Serre, *Adv. Funct. Mater.* **2023**, *34*, 2309089.
[27] F. Lorignon, A. Gossard, M. Carboni, *J. Chem. Eng.* **2020**, *393*, 124765.
[28] M. Zou, M. Dong, T. Zhao, *Int. J. Mol. Sci.* **2022**, *23*, 9396.
[29] F. Ahmadijokani, H. Molavi, M. Rezakazemi, S. Tajahmadi, A. Bahi, F. Ko, T. M. Aminabhavi, J. R. Li, M. Arjmand, *Prog. Mater. Sci.* **2022**, *125*, 100904.
[30] E. Haque, J. W. Jun, S. H. Jhung, *J. Hazard. Mater.* **2011**, *185*, 507–511.
[31] C. F. Pereira, A. J. Howarth, N. A. Vermeulen, F. A. A. Paz, J. P. C. Tomé, J. T. Hupp, O. K. Farhace, *Mater. Chem. Front.* **2017**, *1*, 1194–1199.
[32] A. Khutia, H. U. Rammelberg, T. Schmidt, S. Henninger, C. Janiak, *Chem. Mat.* **2013**, *25*, 790–798.
[33] C. Janiak, *J. Chem. Soc., Dalton Trans.* **2000**, *21*, 3885–3896.
[34] J. Zhang, L. Peng, G. Li, A. Kushwaha, M. Muddassir, X. Wang, J. C. Jin, *J. Solid State Chem.* **2023**, *326*, 124220.
[35] G. Han, Y. Du, Y. Huang, S. Yang, W. Wang, S. Su, B. Liu, *Sep. Purif. Technol.* **2021**, *279*, 119718.
[36] Y. Yang, C. Tu, Z. Liu, J. Wang, X. Yang, F. Chen, *Polyhedron* **2021**, *206*, 115339.
[37] R. G. Saratale, S. Sivapathan, G. D. Saratale, J. R. Banu, D. S. Kim, *Ecotoxicol. Environ. Saf.* **2019**, *167*, 385–395.
[38] Y. Xie, T. Zhang, B. Wang, W. Wang, *Mater* **2024**, *17*, 1972.
[39] M. Beydaghdari, F. H. Saboor, A. Babapoor, V. V. Karve, M. Asgari, *Energies* **2022**, *15*, 2023.
[40] H. W. Haso, A. A. Dubale, M. A. Chimdesa, M. Atlabachew, *Front. Mater.* **2022**, *9*, 840806.
[41] Y. Li, Z. Xu, W. X. Wang, *J. Chem. Eng.* **2022**, *433*, 134584.
[42] M. Oggianu, F. Manna, S. A. Sahadevan, N. Avarvari, A. Abhervé, M. L. Mercuri, *Crystals* **2022**, *12*, 763.
[43] E. Yılmaz, E. Sert, F. S. Atalay, *J. Taiwan Inst. Chem. Eng.* **2016**, *65*, 323–330.
[44] F. Tan, M. Liu, K. Li, Y. Wang, J. Wang, X. Guo, G. Zhang, C. Song, *J. Chem. Eng.* **2015**, *281*, 360–367.
[45] D. Griffith, K. Krot, J. Comiskey, K. B. Nolan, C. J. Marmion, *Dalton Trans.* **2008**, *1*, 137–147.
[46] N. S. Bedowr, R. B. Yahya, N. Farhan, *J. Saudi Chem. Soc.* **2018**, *22*, 255–260.
[47] G. B. Deacon, R. J. Phillips, *Coord. Chem. Rev.* **1980**, *33*, 227–250.
[48] M. Nara, H. Torii, M. Tasumi, *J. Phys. Chem.* **1996**, *100*, 19812–19817.
[49] A. R. Bagheri, M. Ghaedi, *Arab. J. Chem.* **2020**, *13*, 5218–5228.
[50] A. Khutia, H. U. Rammelberg, T. Schmidt, S. Henninger, C. Janiak, *Chem. Mat.* **2013**, *25*, 790–798.
[51] N. Riezzati, Y. K. Krisnandi, A. Zulys, *IOP Conf. Ser. Mater. Sci. Eng.* **2020**, *902*, 012044.
[52] Y. Yang, C. Tu, Z. Liu, J. Wang, X. Yang, F. Chen, *Polyhedron* **2021**, *206*, 115339.
[53] S. P. Chen, Y. X. Ren, W. T. Wanga, S. L. Gao, *Dalton Trans.* **2010**, *39*, 1552–1557.
[54] C. Xiaoyan, Q. Wang, S. Wang, R. Man, *Polymers* **2020**, *12*, 1905.
[55] H. Kaur, N. Devi, S. S. Siwal, W. F. Alsanie, M. K. Thakur, V. K. Thakur, *ACS Omega* **2023**, *8*, 9004–9030.
[56] C. Odenigbo, Y. Makonnen, A. Asfaw, T. Anastassiades, D. Beauchemin, *J. Anal. At. Spectrom.* **2014**, *29*, 454–457.
[57] W. Ding, J. Yi, X. Wang, L. Shi, Q. Sun, *New J. Chem.* **2021**, *45*, 1309–1316.
[58] P. P. Tumkur, N. K. Gunasekaran, B. R. Lamani, N. Nazario Bayon, K. Prabhakaran, J. C. Hall, G. T. Ramesh, *Nanomanufacturing* **2021**, *1*, 176–189.
[59] H. M. Guerreiro, P. Melnikov, I. Arkhangelsky, L. C. S. de Oliveira, G. A. Wandekoken, V. A. do Nascimento, *Int. J. Developm. Res.* **2021**, *11*, 43318–43321.
[60] A. Ashok, A. Kumar, R. R. Bhosale, M. A. H. Saleh, L. J. Van Den Broeke, *RSC Adv.* **2015**, *5*, 28703–28712.
[61] P. Gibot, L. Vidal, *J. Eur. Ceram.* **2010**, *30*, 911–915.
[62] I. A. Lázaro, *Eur. J. Inorg. Chem.* **2020**, *2020*, 4284–4294.
[63] U. Ulusoy, *Minerals* **2023**, *13*, 91.
[64] P. Hirschle, T. Preiß, F. Auras, A. Pick, J. Völkner, D. Valdepérez, G. Witte, W. J. Parak, J. O. Rädler, S. Wuttke, *Cryst. Eng. Comm.* **2016**, *18*, 4359–4368.
[65] M. T. Postek, *J. Res. Natl. Inst. Stan.* **1994**, *99*, 641.
[66] B. Shirley, E. Jarochowska, *Facies* **2022**, *68*, 7.
[67] A. J. Howarth, A. W. Peters, N. A. Vermeulen, T. C. Wang, J. T. Hupp, O. K. Farha, *Chem. Mat.* **2017**, *29*, 26–39.
[68] X. Pan, Q. Zhu, K. Yu, M. Yan, W. Luo, S. C. E. Tsang, L. Mai, *Next Mater.* **2023**, *1*, 100010.
[69] L. Zhao, D. Si, Y. Zhao, L. Wang, H. An, H. Ye, Q. Xin, Y. Zhang, *Colloids Surf. A: Physicochem. Eng. Asp.* **2022**, *644*, 128876.
[70] J. Nicks,, K. Sasitharan, R. R. Prasad, D. J. Ashworth, J. A. Foster, *Adv. Funct. Mater.* **2021**, *31*, 2103723.
[71] S. Choi, T. Kim, H. Ji, H. J. Lee, M. Oh, *J. Am. Chem. Soc.* **2016**, *138*, 14434–14440.
[72] M. A. Lovette, M. F. Doherty, *Cryst. Growth Des.* **2013**, *13*, 3341–3352.
[73] Y. D. Yolanda, A. B. D. Nandiyanto, *ASEAN J. Sci. Eng.* **2022**, *2*, 11–36.
[74] D. Walter, in *Nanomaterials*, (Ed.: Deutsche Forschungsgemeinschaft), Wiley-VCH Verlag GmbH & Co, Weinheim, **2013**, chapter 1, pp. 9–24.
[75] Y. Han, X. Li, L. Li, C. Ma, Z. Shen, Y. Song, X. You, *Inorg. Chem.* **2010**, *49*, 10781–10787.
[76] H. R. Abid, M. R. Azhar, S. Iglauer, Z. H. Rada, A. Al-Yaseri, A. Keshavarz, *Heliyon* **2024**, *10*, e23840.
[77] N. P. Makhanya, B. Oboirien, N. Musyoka, J. Ren, P. Ndungu, *J. Porous Mater.* **2023**, *30*, 387–401.

[78] R. A. Mayo, K. M. Marczenko, E. R. Johnson, *Chem. Sci.* **2023**, *14*, 4777–4785.
[79] P. M. Thabede, N. D. Shooto, S. J. Modise, *Digest J. Nanomater. Biostruct.* **2023**, *18*, 157–163.
[80] X. Feng, W. Li, L. Yang, T. Song, Z. Xia, Q. Lai, X. Zhou, H. Xiao, C. Liu, *Chem. Commun.* **2022**, *58*, 13503–13506.
[81] Z. Qiuyun, Y. Binbin, T. Yuanyuan, Y. Xianju, Y. Rongfei, W. Jialu, D. Taoli, Z. Yutao, *Green Process. Synth.* **2022**, *11*, 184–194.
[82] K. Irikura, J. B. Silva Flor, R. M. Menezes dos Santos, A. Lachgar, R. C. Galvao Frem, M. V. Boldrin Zanoni, *J. CO2 Util.* **2020**, *42*, 101299.
[83] A. Jeyaseelan, N. Viswanathan, *J. Chem. Eng. Data* **2020**, *65*, 5328–5340.
[84] A. H. Khoshakhlagh, F. Golbabaei, M. Beygzadeh, F. Carrasco-Marín, S. J. Shahtaheri, *RSC Adv.* **2020**, *10*, 35582–35596.
[85] Y. A. Patil, S. S. Ganapati, *Chem. Eng. J. Adv.* **2020**, *3*, 100032.
[86] H. Liu, W. Guo, Z. Liu, X. Li, R. Wang, *RSC Adv.* **2016**, *6*, 105282–105287.
[87] S. Afrin, M. W. Khan, E. Haque, B. Ren, J. Z. Ou, *J. Colloid Interface Sci.* **2022**, *623*, 378–404.
[88] D. Joshy, S. Chakko, Y. A. Ismail, P. Periyat, *Nanoscale Adv.* **2021**, *3*, 6704–6718.
[89] E. N. El Qada, S. J. Allen, G. M. Walker, *J. Chem. Eng.* **2008**, *135*, 174–184.
[90] S. Brunauer, L. S. Deming, W. E. Deming, E. Teller, *J. Am. Chem. Soc.* **1940**, *62*, 1723–1732.
[91] Y. Yang, J. Zhang, L. Xu, P. Li, Y. Liu, W. Dang, *ACS Omega* **2022**, *7*, 9229–9243.
[92] K. S. Sing, R. T. Williams, *Adsorpt. Sci. Technol.* **2004**, *22*, 773–782.
[93] K. O. Iwuozor, J. O. Ighalo, E. C. Emenike, C. A. Igwegbe, A. G. Adeniyi, *J. Chem. Lett.* **2021**, *2*, 188–198.
[94] R. Bardestani, G. S. Patience, S. Kaliaguine, *Can. J. Chem. Eng.* **2019**, *97*, 2781–2791.
[95] M. du Plessis, *Phys. Status Solidi A* **2007**, *204*, 2319–2328.
[96] S. Seifi, D. Levacher, A. Razakamanantsoa, N. Sebaibi, *Appl. Sci.* **2023**, *13*, 5616.
[97] C. Scherdel, G. Reichenauer, M. Wiener, *Microporous Mesoporous Mater.* **2010**, *132*, 572–575.
[98] J. H. De Boer, B. C. Lippens, B. G. Linsen, J. C. P. Broekhoff, A. Van den Heuvel, T. J. Osinga, *J. Colloid Interface Sci.* **1966**, *21*, 405–414.
[99] S. Storck, H. Bretinger, W. F. Maier, *Appl. Catal. A: Gen.* **1998**, *174*, 137–146.
[100] K. S. Sing, *J. Porous Mater.* **1995**, *2*, 5–8.
[101] A. Galarneau, D. Mehlhorn, F. Guenneau, B. Coasne, F. Villemot, D. Minoux, D. Minoux, C. Aquino, J. P. Dath, *Langmuir* **2018**, *34*, 14134–14142.
[102] U. Kuila, M. Prasad, *Lead. Edge* **2013**, *32*, 1478–1485.
[103] L. Desmurs, A. Galarneau, C. Cammarano, V. Hulea, C. Vaulot, H. Nouali, A. Sachse, *Chem. Nano. Mat.* **2022**, *8*, e202200051.
[104] F. Younas, A. Mustafa, Z. U. R. Farooqi, X. Wang, S. Younas, W. Mohy-Ud-Din, M. M. Hussain, *Water* **2021**, *13*, 215.
[105] C. M. Ma, G. B. Hong, Y. K. Wang, *Materials* **2020**, *13*, 2764.
[106] I. Sentürk, M. Alzein, *Acta Chim. Slov.* **2020**, *67*, 55–69.
[107] T. Pernyeszi, R. Farkas, J. Kovács, *Minerals* **2019**, *9*, 555.
[108] C. E. de Farias Silva, B. M. da Gama, A. H. da Silva Gonçalves, J. A. Medeiros, A. K. de Souza Abud, *J. King Saud Univ. Eng. Sci.* **2020**, *32*, 351–359.
[109] T. K. Murthy, B. S. Gowrishankar, R. H. Krishna, M. N. Chandraprabha, B. B. Mathew, *J. Environ. Chem. Ecotoxicol.* **2020**, *2*, 205–212.
[110] D. Robati, S. Bagheriyan, M. Rajabi, O. Moradi, A. A. Peyghan, *Physica E Low Dimens. Syst. Nanostruct.* **2016**, *83*, 1–6.
[111] I. B. Ustunol, N. I. Gonzalez-Pech, V. H. Grassian, *J. Colloid Interface Sci.* **2019**, *554*, 362–375.
[112] M. S. Chiou, H. Y. Li, *J. Hazard. Mater.* **2002**, *93*, 233–248.
[113] F. Sevim, O. Lacin, E. F. Ediz, F. Demir, *Environ. Prog. Sustain. Energy* **2021**, *40*, e13471.
[114] J. P. Vareda, *J. Mol. Liq.* **2023**, *376*, 121416.
[115] W. Rudzinski, W. Plazinski, *J. Phys. Chem. B* **2006**, *110*, 16514–16525.
[116] R. V. Kandisa, N. S. Kv, R. Gopinadh, K. Veerabhadram, *Rasayan, J. Chem.* **2021**, *14*, 1528-1533.
[117] A. Denizli, R. Say, Y. Arica, *Sep. Purif. Technol.* **2000**, *21*, 181–190.
[118] Q. Hu, Z. Zhang, *Environ. Sci. Pollut. Res.* **2020**, *27*, 43865–43869.
[119] F. C. Wu, R. L. Tseng, S. C. Huang, R. S. Juang, *J. Chem. Eng.* **2009**, *151*, 1–9.
[120] Y. S. Ho, G. McKay, *Process Saf. Environ. Prot.* **1998**, *76*, 332–340.
[121] H. Grabi, A. Ouakouak, S. Kadouche, W. Lemlikchi, F. Derridj, A. T. M. Din, *Surf. Interfaces* **2022**, *30*, 101947.
[122] L. Zhang, M. Jaroniec, *Interface Sci. Technol.* **2020**, *31*, 39–62.
[123] M. Doğan, M. H. Karaoğlu, M. Alkan, *J. Hazard. Mater.* **2009**, *165*, 1142–1151.
[124] M. A. Rauf, S. B. Bukallah, F. A. Hamour, A. S. Nasir, *J. Chem. Eng.* **2008**, *137*, 238–243.
[125] M. Alkan, Ö. Demirbaş, M. Doğan, *Microporous Mesoporous Mater.* **2007**, *101*, 388–396.
[126] A. Mittal, A. Malviya, D. Kaur, J. Mittal, L. Kurup, *J. Hazard. Mater.* **2007**, *148*, 229–240.
[127] V. K. Gupta, A. Mittal, L. Kurup, J. Mittal, *J. Colloid Interface Sci.* **2006**, *304*, 52–57.
[128] W. H. Cheung, Y. S. Szeto, G. McKay, *Bioresour. Technol.* **2007**, *98*, 2897–2904.
[129] I. Langmuir, *J. Am. Chem. Soc.* **1916**, *38*, 2221–2295.
[130] P. Thilagavathy, T. Santhi, *Chin. J. Chem. Eng.* **2014**, *22*, 1193–1198.
[131] B. Singha, S. K. Das, *Colloids Surf. B: Biointerfaces* **2013**, *107*, 97–106.
[132] E. Alver, A. Ü. Metin, *J. Chem. Eng.* **2012**, *200*, 59–67.
[133] T. A. Khan, S. Sharma, I. Ali, *Toxicol. Environ. Health Sci.* **2011**, *3*, 286–297.
[134] G. Garcıa, A. Faz, M. Cunha, *Int. Biodeterior. Biodegrad.* **2004**, *54*, 245–250.
[135] W. Jianlong, Z. Xinmin, D. Decai, Z. Ding, *J. Biotech.* **2001**, *87*, 273–277.
[136] C. H. Sheindorf, M. Rebhun, M. Sheintuch, *J. Colloid Interface Sci.* **1981**, *79*, 136–142.
[137] T. A. Saleh, *Interface Sci. Technol.* **2022**, *34*, 65–97.
[138] J. Liu, X. Wang, *Sci. World* **2013**, *6*, 897159.
[139] A. A. Inyinbor, F. A. Adekola, G. A. Olatunji, *S. Afr. J. Chem.* **2016**, *69*, 218–226.
[140] F. Brouers, T. J. Al-Musawi, *J. Mol. Liq.* **2015**, *212*, 46–51.
[141] O. J. D. L. Redlich, D. L. Peterson, *J. Phys. Chem.* **1959**, *63*, 1024–1024.
[142] J. Wang, X. Guo, *Chemosphere* **2020**, *258*, 127279.
[143] M. A. Hossain, H. H. Ngo, W. S. Guo, T. V. Nguyen, *Bioresour. Technol.* **2012**, *113*, 97–101.
[144] B. Subramanyam, A. Das, *J. Environ. Health Sci. Eng.* **2014**, *12*, 1–6.
[145] P. S. Kumar, S. Ramalingam, C. Senthamarai, M. Niranjanaa, P. Vijayalakshmi, S. Sivanesan, *Desalination* **2010**, *261*, 52–60.
[146] I. Tosun, *Int. J. Environ. Res. Public Health* **2012**, *9*, 970–984.
[147] M. A. Al-Ghouti, D. A. Da'ana, *J. Hazard. Mater.* **2020**, *393*, 122383.
[148] A. M. Carvajal-Bernal, F. Gomez-Granados, L. Giraldo, J. C. Moreno-Pirajan, *Eur. J. Chem.* **2017**, *8*, 112–118.
[149] R. Saadi, Z. Saadi, R. Fazaeli, N. E. Fard, *Korean J. Chem. Eng.* **2015**, *32*, 787–799.
[150] I. Salahshoori, M. N. Jorabchi, S. Ghasemi, S. M. S. Mirnezami, M. A. Nobre, H. A. Khonakdar, *J. Water Process Eng.* **2023**, *55*, 104081.
[151] A. Sharma, A. Choudhry, B. Mangla, S. A. Chaudhry, *Clean Technol. Environ. Policy.* **2024**, *26*, 39213935.
[152] Y. Li, C. Gao, J. Jiao, J. Cui, Z. Li, Q. Song, *ACS Omega* **2021**, *6*, 33961–33968.
[153] R. H. Ellerbrock, H. H. Gerke, *J. Plant Nutr. Soil Sci.* **2021**, *184*, 388–397.
[154] F. Mashkoor, A. Nasar, *J. Magn. Magn. Mater.* **2020**, *500*, 166408.
[155] X. S. Hu, R. Liang, G. Sun, *J. Mater. Chem. A* **2018**, *6*, 17612–17624.
[156] M. Karnib, A. Kabbani, H. Holail, Z. Olama, *Energy Procedia* **2014**, *50*, 113–120.
[157] Q. Fu, J. Lou, R. Zhang, L. Peng, S. Zhou, W. Yan, C. Mo, J. Luo, *J. Solid State Chem.* **2021**, *294*, 121836.
[158] M. Vakili, S. Deng, G. Cagnetta, W. Wang, P. Menga, D. Liub, G. Yub, *Sep. Purif. Technol.* **2019**, *224*, 373–387.
[159] Z. Zaidi, A. Manchanda, A. Sharma, A. Choudhry, M. Sajid, S. A. Khan, A. Khan, S. A. Chaudhry, *Chem. Eng. J. Adv.* **2023**, *16*, 100571.
[160] A. A. Brouziotis, A. Giarra, G. Libralato, G. Pagano, M. Guida, M. Trifuoggi, *Front. Environ. Sci.* **2022**, *10*, 948041.
[161] I. Blinova, M. Muna, M. Heinlaan, A. Lukjanova, A. Kahru, *Nanomaterials* **2020**, *10*, 328.
[162] Y. An, X. Lv, W. Jiang, L. Wang, Y. Shi, X. Hang, H. Pang, *Green Chem. Eng.* **2024**, *5*, 187–204.
[163] P. Turcotte, S. A. Smyth, F. Gagné, C. Gagnon, *Toxics* **2022**, *10*, 254.
[164] Z. Huang, F. Zhao, L. Fan, W. Zhao, B. Chen, X. Chen, S. F. Zhou, J. Xiao, G. Zhan, *Mater. Des.* **2020**, *194*, 108881.
[165] M. Ding, X. Cai, H. L. Jiang, *Chem. Sci.* **2019**, *10*, 10209–10230.
[166] M. Mohammadikish, D. Jahanshiri, *Solid State Sci.* **2020**, *99*, 106063.

[167] N. Sapawe, A. A. Jalil, S. Triwahyono, M. I. A. Shah, R. Jusoh, N. F. M. Salleh, A. H. Karim, *J. Chem. Eng.* **2013**, *229*, 388–398.
[168] S. W. Lv, J. M. Liu, H. Ma, Z. H. Wang, C. Y. Li, N. Zhao, S. Wang, *Microporous Mesoporous Mater.* **2019**, *282*, 179–187.
[169] W. Zuo, Y. Fan, L. Yang, L. Cui, *J. Inorg. Organomet. Polym. Mater.* **2020**, *30*, 2105–2113.
[170] M. Muslim, A. Ali, I. Neogi, N. Dege, M. Shahid, M. Ahmad, *Polyhedron* **2021**, *210*, 115519.
[171] R. L. Tseng, P. H. Wu, F. C. Wu, R. S. Juang, *J. Taiwan Inst. Chem. Eng.* **2011**, *42*, 312–319.
[172] A. W. Marczewski, *Langmuir* **2010**, *26* 15229–15238.
[173] S. Brunauer, P. H. Emmett, E. Teller, *J. Am. Chem. Soc.* **1938**, *60*, 309–319.
[174] X. He, Z. Zhang, in *Proceedings of the 3rd International Conference on Material, Mechanical and Manufacturing Engineering*, Atlantis Press, Guangzhou, **2015**, pp. 1907–1911.
[175] P. Ehiomogue, I. I. Ahuchaogu, I. E. Ahaneku, *Acta Tech. Corviniensis* **2021**, *14*, 87–96.
[176] K. S. Walton, R. Q. Snurr, *J. Am. Chem. Soc.* **2007**, *129*, 8552–8556.
[177] K. S. Sing, *Pure Appl. Chem.* **1985**, *57*, 603–619.
[178] J. C. P. Broekhoff, *Stud. Surf. Sci. Catal.* **1979**, *3*, 663–684.
[179] F. J. Sotomayor, K. A. Cychosz, M. Thommes, *Acc. Mater. Res.* **2018**, *3*, 4–50.
[180] C. H. E. N. Keluo, T. Zhang, C. H. E. N. Xiaohui, H. E. Yingjie, X. Liang, *Pet. Explor. Dev.* **2018**, *45*, 412–421.
[181] E. P. Barrett, L. G. Joyner, P. P. Halenda, *J. Am. Chem. Soc.* **1951**, *73*, 373–380.
[182] B. Ding, W. J. Ong, J. Jiang, X. Chen, N. Li, *Appl. Surf. Sci.* **2020**, *500*, 143987.
[183] H. Nam, E. S. Sim, M. Je, H. Choi, Y. C. Chung, *ACS Appl. Mater. Interfaces.* **2021**, *13*, 37035–37043.
[184] J. Villarroel-Rocha, D. Barrera, K. Sapag, *Microporous and Mesoporous Mater.* **2014**, *200*, 68–78.
[185] J. H. De Boer, B. C. Lippens, B. G. Linsen, J. C. P. Broekhoff, A. Van den Heuvel, T. J. Osinga, *J. Colloid Interface Sci.* **1966**, *21*, 405–414.
[186] A. Galarneau, F. Villemot, J. Rodriguez, F. Fajula, B. Coasne, *Langmuir* **2014**, *30*, 13266–13274.
[187] M. Belhachemi, F. Addoun, *Appl. Water Sci.* **2011**, *1*, 111–117.
[188] S. Azizian, *J. Colloid Interface Sci.* **2004**, *276*, 47–52.
[189] Y. S. Ho, G. McKay, *Process Saf. Environ. Prot.* **1998**, *76*, 332–340.
[190] Y. S. Ho, G. McKay, *Process Biochem* **1999**, *34*, 451–465.
[191] W. J. Weber Jr., J. C. Morris, *J. Sanit. Eng. Div.* **1963**, *89*, 31–59.
[192] K. Y. Foo, B. Hameed, *J. Chem. Eng.* **2010**, *156*, 2–10.
[193] A. O. Dada, A. P. Olalekan, A. M. Olatunya, O. J. I. J. C. Dada, *IOSR J. Appl. Chem.* **2012**, *3*, 38–45.
[194] A. Dąbrowski, *Adv. Colloid Interface Sci.* **2001**, *93*, 135–224.
[195] M. P. Linde, K. Marquez, *KIMIKA* **2021**, *32*, 19–33.
[196] J. Ru, X. Wang, F. Wang, X. Cui, X. Du, X. Lu, *Ecotoxicol. Environ. Saf.* **2021**, *208*, 111577.
[197] V. Russo, M. Trifuoggi, M. Di Serio, R. Tesser, *Chem. Eng. Technol.* **2017**, *40*, 799–820.
[198] S. Rattanapan, J. Srikram, P. Kongsune, *Energy Procedia* **2017**, *138*, 949–954.
[199] S. Rengaraj, Y. Kim, C. K. Joo, K. Choi, J. Yi, *Korean J. Chem. Eng.* **2004**, *21*, 187–194.
[200] A. V. Kiselev, *Kolloid Zhur* **1958**, *20*, 338–348.
[201] M. Davoudinejad, S. A. Ghorbanian, *Sci. Res. Essays* **2013**, *8*, 2263–2275.
[202] R. Sips, *J. Chem. Phys.* **1948**, *16*, 490–495.
[203] L. T. Popoola, *Heliyon* **2019**, *5*, e01143.
[204] A. H. Khoshakhlagh, F. Golbabaei, M. Beygzadeh, F. Carrasco-Marín, S. J. Shahtaheri, *RSC Adv.* **2020**, *10*, 35582–35596.

Manuscript received: June 8, 2024